Understanding DNA Electrophoresis in Colloidal Crystals

A DISSERTATION
SUBMITTED TO THE FACULTY OF THE
UNIVERSITY OF MINNESOTA
BY

Scott Bradley King

IN PARTIAL FULFILLMENT OF THE REQUIREMENTS
FOR THE DEGREE OF
Doctor of Philosophy

Kevin D. Dorfman

August, 2014

Acknowledgements

I would like to thank my wife, for the support she has shown throughout my entire PhD. I would also like to thank my advisor, Kevin Dorfman, for sticking with me throughout all the seasons of my research. This work was supported by the David and Lucile Packard Foundation, NSF Grant CBET-0642794, and NIH R01-HG005216. Portions of this work were performed in the University of Minnesota NanoFabrication Center, which receives partial support from the NSF through the NNIN. I thank Neda Nazemifard for her insights into controlling successful colloidal self-assembly and device preparation and Patrick F. Mooney for contributing the Python script used to combine position and intensity data.

The text of Chapter 3 is derived from my paper which appeared in *Analytical Chemistry* in 2013.

Dedication

This Thesis and my PhD are dedicated to my family, starting with my son Caleb Everett and wife Kathryn Elizabeth. You are the reason I work.

Abstract

The electrophoretic separation of DNA (deoxyribose nucleic acid) has been a target of engineering and optimization since its inception. In the following pages, I describe an engineering investigation into the physics of DNA separation in colloidal crystals. Colloidal crystals are formed through self-assembly of micron-sized spheres, suspended as a colloidal suspension. In this work, I follow the pioneering separation work of Zeng and Harrison, seeking to better understand the properties that allow for the observed enhanced separations of small, <1 kilo base-pair (kbp) DNA and large (>10 kbp) DNA. I demonstrate some key insights required to fabricate these devices, then move on to evaluating their performance. In the first section I tackle the quality of the crystal and its potential effects on separation performance. In the second section, I attempt to explain the order of magnitude better separation behavior between agarose gels and colloidal crystals by evaluating the mobility regimes for large DNA. At the end of this work, I have included a discussion on the future place of colloidal crystals as a separation medium.

Contents

List of Tables

List of Figures

Chapter 1

DNA in Colloidal Crystals

1.1 Outline of the Thesis

My thesis journey began in the fall of 2008, but that is not where my research story begins. Chapter 1 describes the history of the key elements of my thesis: DNA separations and colloidal crystals. It concludes with a review of the work so far towards combining these elements. Chapter 2 is a comprehensive walkthrough of my experimental process, including a discussion of various failure mechanisms and how to avoid them. This chapter is designed as a manual for future experimentalists who wish to follow in my footsteps.

Chapters 3 and 4 are the published work and results of my thesis. The first paper, Chapter 3, originally included a Supplemental Information section. The SI information has been rewritten back into the paper as it was originally intended. Chapter 4 was prepared for publication and is presented in an adaptation of that format.

Finally, Chapter 5 begins with a discussion of the process involved in developing my unique measurement techniques and analysis methods. I include a brief roadmap for continuance of my projects, and end with a discussion of the projected impacts and importance of the discoveries contained within this thesis. This thesis serves as both a manual for a journal of research on DNA electrophoresis in colloidal crystals.

1.2 Introduction to DNA separation

Deoxyribose nucleic acid (DNA) is known as the "molecule of life". It is a biopolymer made of four primary building blocks, the bases adenine (A), thymine (T), guanine (G), and cytosine (C) joined together with a phosphate-sugar backbone. In its double-stranded form (most commonly found in the cell nucleus, packed into chromosomes), the two DNA strands

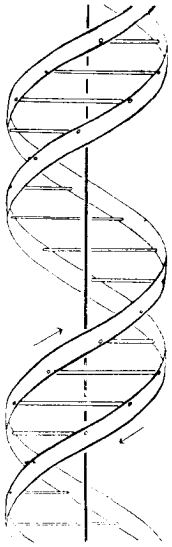

Figure 1.1: The original proposed schematic for the double-stranded structure of DNA by Watson and Crick [1]. They made key insights by working with toy models, the x-ray diffraction data of Rosalind Franklin, and the observation of unity base ratios (indicating base pairs) from Zamenhof *et al.* [2]. Adapted from Ref. [1].

are anti-parallel, with the bases paired with their complement: adenine with thymine, guanine with cytosine. These are called basepairs, and are considered the primary unit of the DNA chain. The pairing allows for easy duplication of the DNA: the strands are unzipped, and new strands are polymerized from free nucleotides. The result is two perfect copies of the original chain, and is part of what makes the information transfer of life possible.

The DNA of a healthy human is contained within their cell nuclei in the form of 23 chromosome pairs: one set from the mother, and one from the father. These chromosomes are tightly-wrapped bundles of DNA, ranging roughly from 48 to 249 megabasepairs (Mbp) and are depicted in Figure 1.1. Geneticists further break down chromosomes into genes, which are sections of the DNA that are used by the cell to perform specific tasks. These genes can be anywhere from <1 kilobasepair (kbp) up to >2 Mbp in length, and are often the targets in todays world of personalized medicine and gene therapy treatments. Finally, within these genes are three-base sequences used as unique identifiers during DNA transcription into proteins, called codons. The DNA molecule contains information at every level of its structure that is used by the cell to determine its function, efficiency, and even its deficiencies, all of which have lead to DNA being a key object of study since its discovery.

"DNA separation" refers to the isolation of differently-sized fragments of DNA. These

fragments can be created through various means, however in most analytical uses the cause of fragmentation is purposeful "cutting" of the DNA through the use of restriction enzymes [12]. These enzymes are designed to target specific sequences of DNA bases, generally no longer than a dozen bases. When the source DNA molecule is very long, it is probable that these targeted sequences will appear multiple times. After the enzyme "restricts" the DNA, it will leave multiple strands of various lengths behind. To determine the resultant distribution of lengths, one needs to separate the mixture by size. This is most readily understood in the context of "DNA fingerprinting," as seen on numerous crime shows. When an individual's DNA is subjected to a standardized battery of restriction enzymes, the resultant distribution of molecular sizes will be largely unique to that individual. However, because it pertains to the DNA sequence, it can also show hereditary links, as DNA will have similarities between parent and offspring. It is important to note that the DNA sequences targeted for forensic study are repeat-rich and highly variable, allowing for both repeatable results and unique outcomes for individuals.

The separation of DNA is commonly eluted electrophoretically because the DNA phosphate backbone has an overall negative charge when in solution. Therefore, under the presence of an applied electric field, the DNA molecule will be electrophoretically driven towards the anode.[1] The cathode and anode used in electrophoresis are reactive and induce an ionic current in the buffer which carries the electric field. The charge of a DNA molecule is linearly proportional to its length (the number of base-pairs), and so one may think that separation would occur naturally: larger molecules move faster, as they experience a higher pulling force. However, the molecule is not floating in a vacuum, and the buffer solution the DNA is in provides both friction and counterion flow. In the case of large, coiled DNA in a good solvent, the DNA molecule will produce an electroosmotic drag proportional to its length and opposite its own motion. The result is an electrophoretic mobility in free solution that is independent of DNA size, and therefore yields no size separation [4].

The solution to this problem is to break the balance in the stall force. This was first done for DNA using loose agarose gels in 1972 [13]. Agarose gels are formed by superheating solutions of a basic buffer and agarose (a natural polymer found in seaweed) and then allowing them to cool. The agarose crosslinks, forming a self-supporting fiber network in an electrolyte solution. The network is generally described as a porous network (filling fractions $< 5\%$) with a statistical average pore size. This average pore size is linearly proportional to the concentration of agarose used to cast the gel. DNA, when travelling through the

[1] As "cathode" and "anode" can have different definintions depending on the background of the reader, the anode as described in this thesis will be the positive, higher-potential terminal.

gel, still experience a pulling force linearly related to the molecule size. However, they are retarded by the gel in a size-dependant manner, depicted in Figure 1.2 [4]. In the case of small DNA in low electric fields, this retardation effect is described well by the Ogston sieving model [14–16], where the electrophoretic mobility is proportional to the free volume available to the molecule, which exponentially decays as the molecule increases in size. DNA much larger than the pore size of the gel has a mobility that decreases inversely with the size of the molecule. However, this is only seen in the "biased reptation" regime, where the large DNA moves through the gel in a loosely-coiled configuration. The chain slides through a conceptual "tube" that is itself in a coiled conformation as shown in Figure 1.3. The motion of the DNA through this tube resembles a slithering snake, hence "reptation". When the electrophoretic driving force is too large, one enters the "biased reptation with orientation" regime, and the DNA begins to move in a nearly straight tube towards the anode. While the drag force remains linearly proportional to the chain size, the tube no longer adopts a random coil configuration and the overall mobility becomes independent of the DNA size. The crossover between these regimes in gels occurs at low electric fields ($\sim$1 V/cm or less, depending on gel concentration), which makes separation of DNA molecules $>$10 kbp difficult using direct current (dc) electric fields. This was overcome by periodically pulsing the electric field and allowing for relaxation of the molecule. However, this process significantly increased the separation time, requiring hours to days to separate large DNA. This primary shortcoming of gel electrophoresis has driven much of the work in microfluidic DNA separation platforms [11].

The theories for DNA mobility in gels are mature, refined through careful experiments, detailed models, precise computational experiments, and time [4]. The various mobility regimes, their applicable size and field ranges, and their strengths and weaknesses are fairly well-developed [4]. This has lead to many new technologies being first described through comparisons to gels, a practice that in the case of colloidal crystals has probably hindered their comprehension, rather than assist it. What remains universal in all sieving matrices is a need to break the symmetry between the electrophoretic driving force and the drag force.

1.3 Colloidal Crystals

Colloidal crystals are close-packed structures with colloidal particles as the building block [17]. Prior to crystallization, these building blocks (generally spheres) are suspended in a solution. Two of the most common colloids used in the DNA separation literature are polystyrene and silica colloids [8, 9, 18–23]. The initial investigations into colloidal crystals

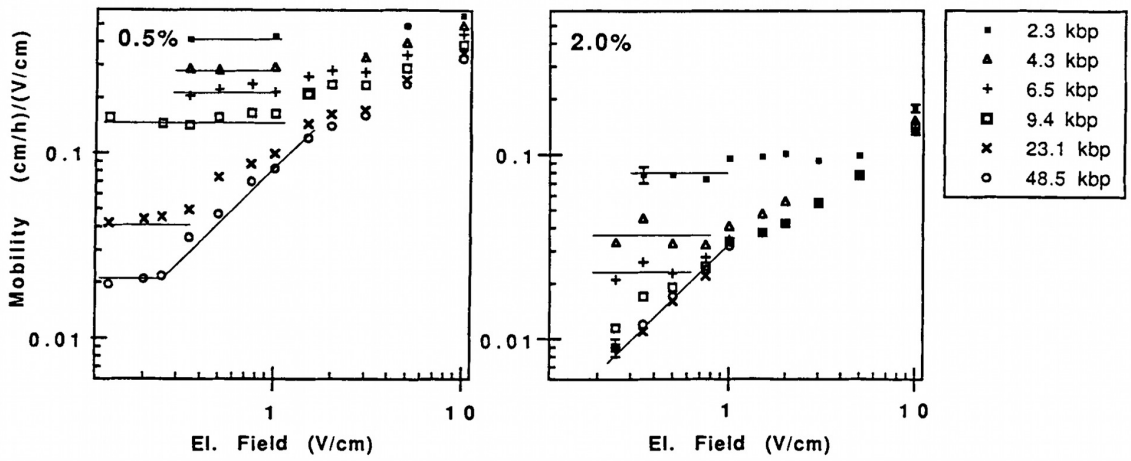

Figure 1.2: Relationship between agarose pore size, DNA molecule size and electric field used to determine molecule mobility during electrophoretic separation [3]. These plots show the lowest and highest gel concentrations tested by Heller *et al.*, 0.5% and 2.0%. They depict separable electric field ranges where each size DNA has a unique mobility value as well as fields that cannot produce separations. In the higher concentration agarose (tighter pores), the separable region is compressed to lower values of the electric field. Adapted from Ref. [3].

were done by groups interested in their optical properties [5]. Briefly, when there exists an index of refraction mismatch between the colloid material and the interstitial medium (air, a solution, or another solid), one observes a periodic index of refraction. The periodicity of this arrangement allows the crystal to only transmit light whose wavelength is a match to the crystal periodicity, essentially acting as a light signal filter [24]. Therefore, much of the initial work in colloidal crystals was towards development of photonic crystals.

A key enabling feature of colloidal crystals is that they self-assemble into close-packed structures (see Figure 1.4). This process is called "colloidal self-assembly" (CSA) [17]. Historically, the photonic crystals were formed on the same silicon wafers used in the microelectronics industry due to their near atomically flat surfaces [5]. These wafers were then dipped in colloidal suspensions of sub-micron particles in aqueous solutions, and evaporation was allowed to proceed. As the water surface lowers, the colloids are drawn to the negative curvature of the wetted surface of the silicon wafer, where evaporative and convective forces pack them together in a close-packed structure. The explanation for such reproducible crystallization was put forth by Norris *et al.* [25] as convective flow through the existing crystal naturally passing through existing interstitial sites. This grows the crystal in close-packed layers, directly analogous to those in an fcc or hcp atomic crystal. Another route towards colloidal crystals is sedimentation [17]. Once again, a flat substrate

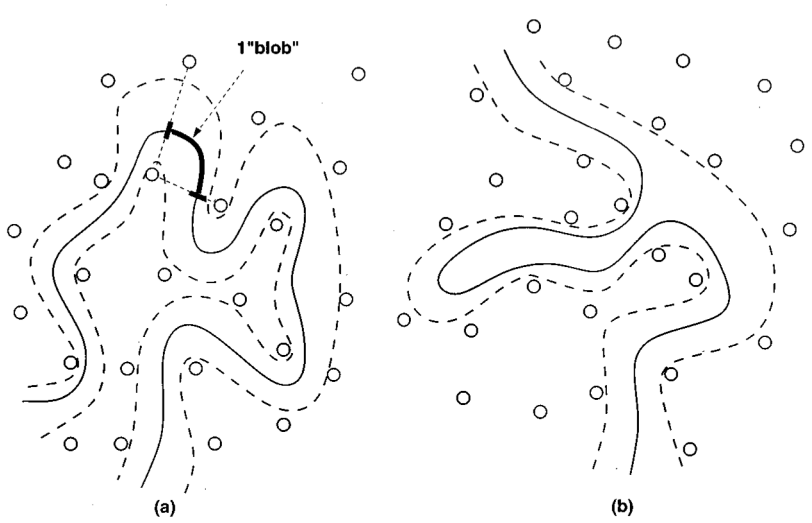

Figure 1.3: A schematic from Viovy [4] depicting two types of DNA reptation through a tube. In (a) the DNA molecule (solid line) exists within the conceptual tube (dashed lines) that is bounded by the gel fibers (circles) without herniation. The molecule in (b) has herniated its tube. The "blob" referred to in (a) is the mathematical construct used when dealing with long chains, and is the statistical amount of real chain needed to appear as a monomer of a zoomed-out, abstract chain. Adapted from Ref. [4].

would be used and a colloidal suspension was allowed to settle onto the substrate. During this settling process, the colloids again find a close-packed arrangement to rest in, growing vertically in a layer-by-layer process of close-packed layers.

Spontaneous crystallization was found to require monodisperse colloids with a narrow size distribution [17]. Much like atomic crystals, large size mismatches cause disturbances in the crystal lattice, resulting in a loss of the close-packed nature of the crystal. Also analogous to atomic crystals, colloidal crystals require slow growth to achieve best results [17]. Quickly grown crystals are prone to defects, since each individual colloid has less time to locate an optimal spot. This is less of a problem in CSA, since the same convection driving growth also drives the colloids to open locations [25]. This has led CSA to be the predominant method for colloid crystal fabrication.

The desire to use photonic crystals as waveguides led the Whitesides group to first attempt to grow colloidal crystals inside of microfluidic channels in a process they termed "micromolding in capillaries" (MIMIC) [6]. In these cases, the convective force used was an evaporative flow. The group filled part of their channels with colloidal suspension, then cap the inlet. All evaporation then drives a flow towards the outlet. The fluid flow drives colloids towards the air-liquid-channel interface, where they begin piling up akin to CSA. The result

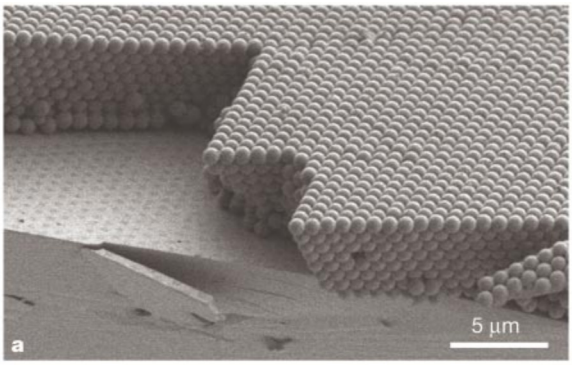

Figure 1.4: A colloidal crystal formed by evaporation-assisted self-assembly of 855 nm diameter silica colloids on a flat silicon wafer substrate [5]. Note the fcc packing, as well as the tendency for the close-packed (111) plane to grow parallel to the flat surface. Adapted from Ref. [5].

after removing the microchannels (formed in the soft material polydimethylsiloxane, PDMS) was patterned photonic crystals, shown in Figure 1.5. Their method proved robust and adaptable, and was used as the basis for creating most of the colloidal crystal networks used for DNA electrophoresis.

The close-packed network is straightforward to visualize for crystallography students, as it has been reproduced in hard-sphere cartoons in most discussions of atomic lattices. In practice, it has been shown that most CSA-grown crystals tend towards fcc packings, but are more commonly random close-packed (rcp) structures [25]. However, since we wish to discuss their utility as DNA electrophoretic sieves, we will need a better understanding of the interstitial space between colloids. This space is much more difficult to picture, and I have been unable to conceive of a satisfactory schematic of it. However, the most common tool for understanding the free space available comes by thinking about the largest spheres that fit in various spaces. In an fcc crystal, there are three main types of interstitial spaces: octahedral sites (bounded by six colloids), tetrahedral sites (bounded by four colloids), and throats (bounded by three touching colloids), all shown schematically in Figure 1.6. The largest spheres that fit in these, given in terms of fractions of the colloid diameter, d: $0.415d$, $0.225d$, and $0.155d$, respectively [7].

These free space analogies are used in the colloidal crystal DNA literature as the point of reference for comparisons to agarose gels [9]. In contrast to the random networks of mostly open space in agarose (>95%), colloidal crystals are mostly filled space (close-packing by definition has a packing fraction of 74%) distributed in a regular, repeated manner. Also, colloidal crystals have much higher mechanical stability than agarose gels, which tend

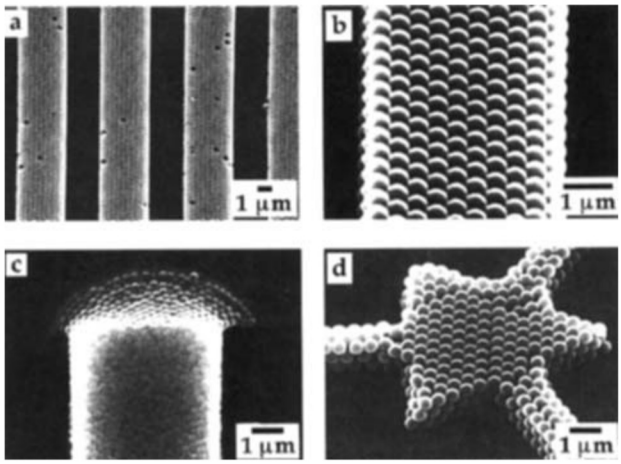

Figure 1.5: The Whitesides group pioneered the field of growing colloidal crystals in microchannels [6]. The figure above displays some of the patterns they achieved using PDMS channels and 0.45 μm diameter polystyrene colloids. Adapted from Ref. [6].

to collapse under their own weight when formed from too-low concentrations, or handled roughly. These quick comparisons were what led to the first investigations of colloidal crystals as replacements for agarose gels in the separation of DNA [8].

1.4 DNA in Colloidal Crystals

The first published work utilizing DNA within a colloid crystal was done by Meistermann and Tinland in 2000 [8]. They created colloidal crystals through sedimentation between two coverslips, confirming the presence of a crystal through laser diffraction. Laser diffraction again plays on the analogy between colloidal crystals and atomic crystals. Much like X-ray diffraction of atomic structures, laser diffraction uses light with a wavelength commensurate with the interplanar spacing of the crystal to create periodic diffraction patterns. In Meistermann and Tinland's study, they performed laser diffraction akin to small-angle X-ray scattering: by aiming the laser beam perpendicular to the close-packed planes, they measured a diffraction pattern with hexagonal symmetry (Figure 1.7). This diffraction pattern is indicative of a rcp crystal, and also indicated crystal grains larger than the laser beam width. They electrophoresed DNA through the crystal and measured the speed of λ-DNA as it moved through the crystal under varying high electric fields (the relative term "high" is used to describe fields many times higher than the fields commonly utilized in agarose gels of 1-10 V/cm). λ-DNA is used throughout the literature as a model large DNA molecule. Taken from the λ-phage bacterium, it is 48.5 kbp long and is able to be mass produced with

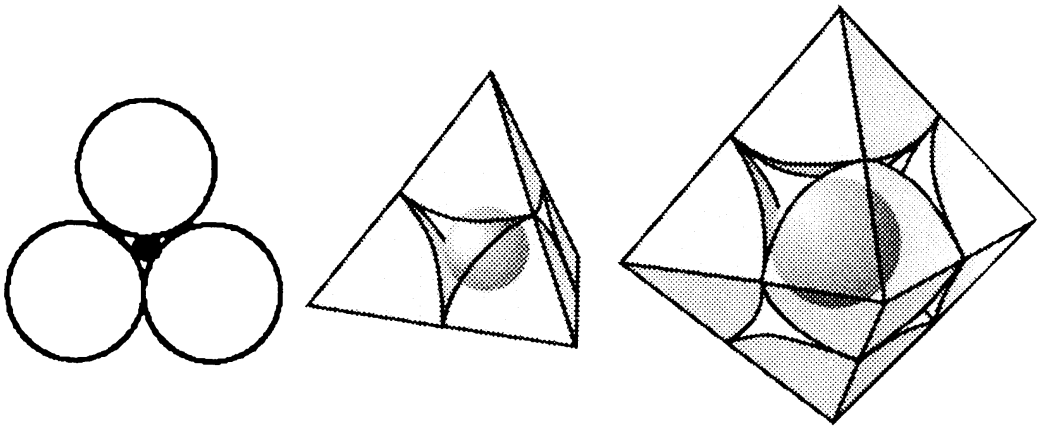

Figure 1.6: A schematic of the three interstitial sizes found within close-packed systems. From left to right, trigonal, tetragonal and octahedral coordination [7]. The largest spheres that can fill these interstitial spaces, in terms of the colloid diameter, d, are $0.155d$, $0.225d$, and $0.415d$ respectively. These comparisons can aid visualization of the interstitial space, but DNA is a flexible polymer and therefore not as limited as touching hard spheres when filling a cavity. Adapted from Ref. [7].

high accuracy and bought at a low price from numerous manufacturers. This has lead to its ubiquity in nearly all work on separating "large" DNA. Meistermann and Tinland also showed that despite the negative surface charges on the colloids in the high pH buffers used for DNA electrophoresis, there was not a prohibitive amount of electroosmotic flow counter to the DNA progress. This effect has remained largely unglamorized, but requires noting for its future relevance in this thesis.

This first use of microfluidics in conjunction with DNA separation and colloidal crystals was done by Zeng and Harrison in 2007 [9]. They used the CSA techniques initially developed by Whitesides to create colloidal crystals inside of a microfluidic channel with a simple cross injection design seen in Figure 1.8. Their key development was in carefully controlling the growth such that the crystal only grew in the separation arm, leaving the injection system clear of any separation medium. This is something that is facile in the standard top-down approaches to microfluidic separation device design, where photolithography is used to pattern devices with posts or other two-dimensional structures at any desired location. The bottom-up approach of CSA required Zeng to monitor growth and terminate it by removing the colloidal suspension from the microfluidic channel in time to stop the growth where desired. Once their system was developed, they showed that colloidal crystals functioned similarly to agarose gels when using small DNA, but with faster and cleaner results. They compared their results to gels using the "pore size" of $0.155d$,

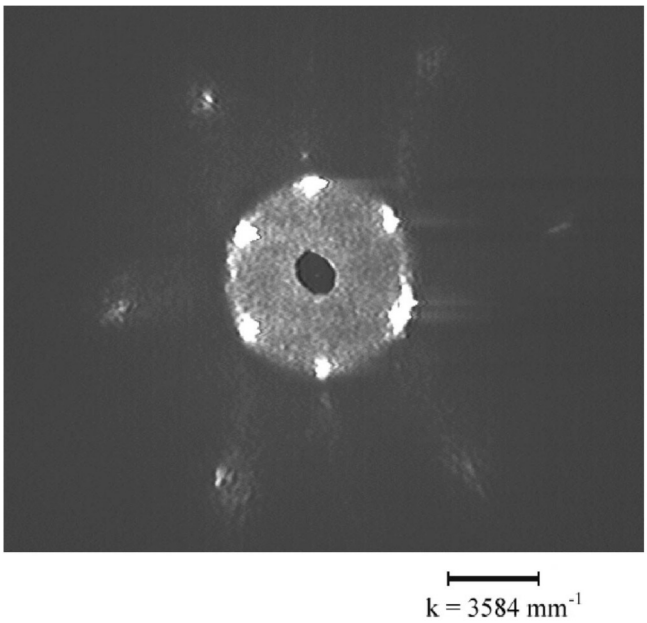

Figure 1.7: The laser diffraction of 488 nm light incident normal to the colloidal crystal (1 μm silica colloids) used by Meistermann and Tinland to study DNA electrophoresis [8]. The scale bar is in wavenumber units, where $k = (4\pi/\lambda)\sin(\theta/2)$, where λ is the light wavelength and θ the scattering angle. The hexagonal symmetry is indicative of random close-packing of the colloids. Adapted from Ref. [8].

the throat formed from three touching colloids. They were also able to separate λ-DNA from calf thymus DNA (a mixture of sizes distributed around 13 kbp) in 900 nm diameter colloids with an electric field an order of magnitude higher than would be required in a gel. They extended these results by separating λ-DNA from T4 DNA (166 kbp) by simply increasing the colloid diameter to 1.6 μm, with the resulting separation shown in Figure 1.9. They based these results on the scaling theories for gels, in which the reptation crossover to orientation can be shifted lower by increasing the pore size [3].

After their paper, Zeng and Harrison went on to adapt colloidal crystals to a continuous separation device, called the "DNA prism" [18, 21]. The DNA was streamed into a crystal with two applied electric fields oriented at an obtuse angle to each other, pulsed as a square wave, and with unique field strengths. In general, larger DNA take longer to reorient, and therefore have a lower angle of deflection from the injection axis than small DNA, which could rapidly reorient in the switching fields. They used these devices to study the effects of creating colloidal crystals with bidisperse colloid sizes on the DNA separation behavior, finding that separation characteristics performed worse than Vegard's Law (properties proportional to component fractions) would predict for mixtures of two colloid sizes [19].

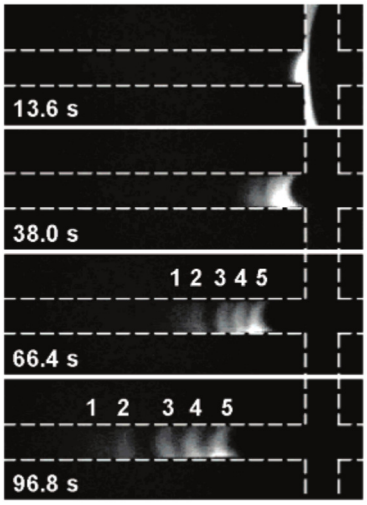

Figure 1.8: An injection within Zeng and Harrison's microfluidic device which utilizes a cross-T injection. The DNA is dyed with YOYO-1 dye. The mixture is labeled 1-5 (200, 400, 800, 1200 and 2000 bp fragments) and separates within 65 s. The channel is $\sim$100 μm wide, which is superimposed on the fluorescence image. Adapted from Ref. [9].

In 2005 Mary Wirth's group evaluated the electromigration of single molecules of DNA in small colloidal crystals [22]. Their work led them to attempt the use of colloidal crystals to separate proteins [23], a process which faces similar challenges to DNA electrophoresis of short chains. Coming from an analytical chemistry perspective, they highlighted the advantages of using close-packed crystal structures instead of the random, loose-packing of most packed-bed separation columns. Using crystals grown via sedimentation in a fused silica capillary (shown in Figure 1.10), they highlighted the extremely low plate heights of the separations – they observed nearly no seive-induced band broadening [20]. They attributed these successes to the close-packing of the crystals, and have continued to apply colloidal crystals as prime protein and DNA separation sieves [10, 26]. Mary Wirth has started a company, bioVidria, to make and sell colloidal crystal-packed separation columns for ultra-high performance liquid chromatography that capitalizes on the low plate heights.

In each of the previous studies, the researchers highlighted the many advantages of colloidal crystals have over traditional gel-based sieves. Colloidal crystals are more mechanically stable, can be easily used over a wide range of DNA sizes, and are well-ordered and therefore introduce less dispersion. They seem capable of performing separations orders of magnitude faster than gels, and can theoretically be integrated into more complicated microfluidic designs. However, they have not seen widespread adoption in the field. In the decade and a half since Meistermann and Tinland first demonstrated them, research has

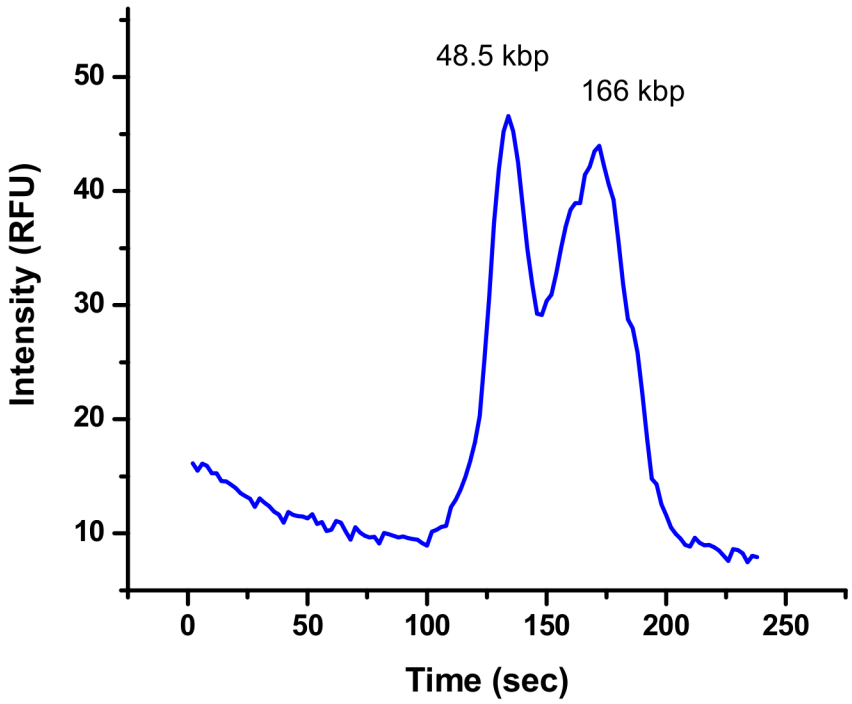

Figure 1.9: Separation of λ (48.5 kbp) and T4 (166 kbp) DNA in 1.53 μm polystyrene colloids. Zeng and Harrison used a field of 14 V/cm and achieved this separation at an elution length of only 1.5 mm. Adapted from Ref. [9].

been reported only in the small handful of studies described above. Additionally, many of the startling results remain insufficiently explained, such as the curiously high fields able to separate λ- and calf thymus DNA. Even from an engineering perspective, I have not seen any examples of colloidal crystals being integrated into any complex devices, unlike micro-fabricated post arrays. In this thesis, I apply an engineer's eye to using colloidal crystals as DNA sieves, and doing so will shed light on their future.

1.5 Focus of the Thesis

The first question that I tackle is the matter of crystal quality. In the established colloidal crystal DNA separation literature, there have been two standards of crystal qualification: SEM images of crystal surfaces [9, 18–23], and laser diffraction of crystalline bulks [8]. I put forth that the common approach, SEM images of surfaces, is not a useful measurement of crystalline quality. For one, it is a measurement of a crystal made outside of the conditions in which it was used to perform the separation. Second, it only images one or two layers deep into crystals that are many tens or hundreds of layers. It is known that most crystalline

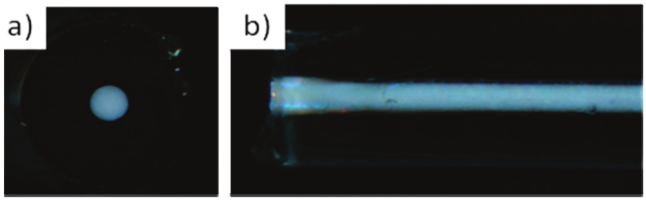

Figure 1.10: Light microscopy images of a silica capillary packed via sedimentation with 330 nm silica colloids [10]. The blue color arises from the Bragg scattering of incident white light on the colloidal crystal. The column is viewed end-on in (a) and alongside in (b). Adapted from Ref. [10].

defects are located more than six layers deep in the crystal [27]. Third, it necessitates the destruction of the device, either after use or of a device that is not used, and therefore may not be useful in a production setting. Far better is the use of laser diffraction. Providing the solvent used to carry the DNA has a different index of refraction from the colloids used, one can take measurements of the crystal *in situ*. The laser diffraction by its nature measures the entire volume of crystal within the beam width. Additionally, it can be easily integrated into an assembly-line process.

The process used to measure crystal quality is important because there are two distinct types of crystals seen in the microfluidic separation literature. Some crystals are comprised of very large grains, with a consistent orientation of the crystal and the electric field, and some are made of many smaller grains, where the orientation of the crystal with the electric field changes often as a molecule moves along the separation channel (see Figure 1.11). This highlights another strength of laser diffraction over SEM measurements. Laser diffraction of a single grain, when perpendicular to the close-packed plane (which generally grows parallel to the channel "floor"), will display a hexagonal pattern of diffraction spots. These spots are a distance from the center proportional to the nearest-neighbor distance in the crystal, and oriented rotationally depending on the orientation of the crystal. If there are two differently-oriented grains illuminated by the beam, the diffraction pattern will have two hexagonal patterns visible rotated with respect to each other. With many different orientations, the diffraction pattern resembles a ring, where the individual hexagonal spots are indistinguishable. In this way, one can rapidly assess if the grains of a the crystal are larger or smaller than the interrogating beam width.

The difference in growing large grains versus small grains is often fine control of the growth rate of the crystal. If the growth rate is fast, one will get many small grains, while slow growth tends to produce large grains. What is not known, is whether there is any effect from the rapidly-switching grain orientation of small grained crystals on the reduced

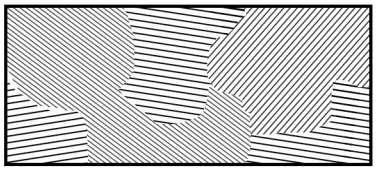

Figure 1.11: In a separation channel with many grains, there will exist texturing – the grains may not all align with the device. In a separation, the applied electric field will always be along the axis of the separation channel. This texturing could have an effect on DNA mobility.

band broadening of the crystal. This question will be answered in the first experimental section of this thesis. Ideally, in commercial use, one desires an insensitivity to grain size, such that large scale fabrication could proceed quickly and with a high acceptance rate of grown crystals.

The second experimental section of this thesis investigates the previously-mentioned startling ability of colloidal crystals to separate large DNA molecules at high electric fields. I work to reproduce the monumental work of Heller *et al.* [3] (see Figure 1.2) to describe the mobility regimes of λ DNA as leverage to explain the surprisingly high separation fields possible for large DNA in colloidal crystals. The comparison between the short DNA, which is commonly used to establish parallels between crystals and agarose gels, and long DNA will highlight where those same parallels break down.

My desire for this thesis is that it will shed light on some of the possible reasons colloidal crystals have not yet lived up to their hype as DNA separation sieves. The reader will leave this manuscript with a greater understanding of the process involved in fabricating these devices as well as assessing their performance. There will also be the development of several new measurement techniques made necessary by some of the challenges faced in using colloidal crystals as DNA electrophoretic sieves and the data required to answer these questions.

Chapter 2

Experimental Background

This chapter serves as a reference for the design, fabrication and use of the microfluidics, colloidal crystals and DNA in the remainder of the thesis. It contains many of the nuances needed to create useable devices that are not published in any literature to date, found through conversations with the original authors as well as my own personal trial and error. Any deviations in subsequent chapters from the methods listed below will be highlighted; otherwise, assume that these were the methods used.

2.1 Microfluidic Device Design

Our research group historically designed its separation devices as shifted-T devices [28]. The shifted-T refers to the injection region of the device. This design in theory provides for a small, easily-controlled injection plug (see Figure 2.1). In the microfluidic studies of Zeng and Harrison [9, 21], the microfluidic channels were made by molding the elastomer PDMS on raised photoresist, patterned in the desired geometry. The photoresist design was created using standard photolithography techniques on Si wafers to pattern a thick resist, which after curing was evaporatively coated with a monolayer of silane, acting to prevent adhesion of the PDMS to the photoresist. The PDMS is then peeled away, leaving the photoresist template free to be reused. Thus removed, the PDMS was then punched through to create access holes to the microchannels prior to bringing the surface in to contact with a glass coverslip. Therefore, the Harrison group would use a setup with three walls of the microchannel formed with PDMS and the fourth wall (or ceiling) being made of glass.

A few of the drawbacks to using a photoresist master are its degradation over time as well as the difficulty in creating thick layers of resist (>10 μm). These were the primary

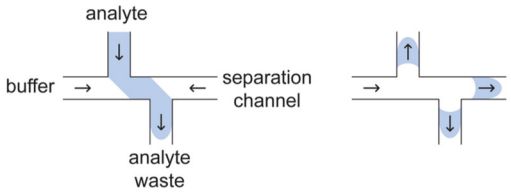

Figure 2.1: The loading and injection scheme of the shifted-T design [11]. The schematic on the left shows the loading scheme, where analyte is drawn into the waste channel until a steady-state analyte concentration is reached. The right side depicts the injection, where analyte is pulled back into the source and waste reservoirs while also being pulled down the separation arm. The shifted-T design allows for control over the width of the injected plug by balancing the pull-back forces of the waste and source reservoirs during injection. This control increases the consistency of the injection width. Adapted from Ref. [11].

reasons I developed my channels to be etched into glass. Using photoresist-coated, chrome-coated glass I first developed my pattern in the resist. The resist then functioned as an etch mask for the Cr-coating, which later functioned as an etch mask for the glass. In this way, I could create reusable glass channels with smooth walls that were much more robust than the PDMS channels. I seal my devices with a flat PDMS lid, cut from a silanized flat silicon wafer, which results in my having three walls of glass and one wall of PDMS.

Additionally, my microfluidic design includes distance markers along the length of the separation arm, shown in Figure 2.2. These markers function both as location indicators when viewed in a microscope, but also as diffraction sources when illuminated by a laser. They function to aid the correlation of laser diffraction data with optical crystalline studies, as well as DNA separation performance.

2.2 Device Fabrication

We fabricated our devices in glass coated with Cr and AZ1518 photoresist from Nanofilm, Inc. AZ1518 is a standard, positive photoresist which develops with Shipley 350 developer. The glass plates used are 5" by 5", the same dimensions as the mask used. However, the MABA-6 mask aligner and UV exposure system only exposes a portion of the mask correlated to a 4" diameter silicon wafer. The mask is exposed to 10 mW near-UV light ($\approx$400 nm wavelength) for 8 seconds. This exposes five identical copies of the channel design for each glass plate used. The exposed wafer is then treated with Shipley 350 developer for 20 seconds, then rinsed in DI water. Being a positive resist, this removes resist in the future etch locations.

The etching process begins with a Cr etch (ceric ammonium nitrate + nitric acid). This

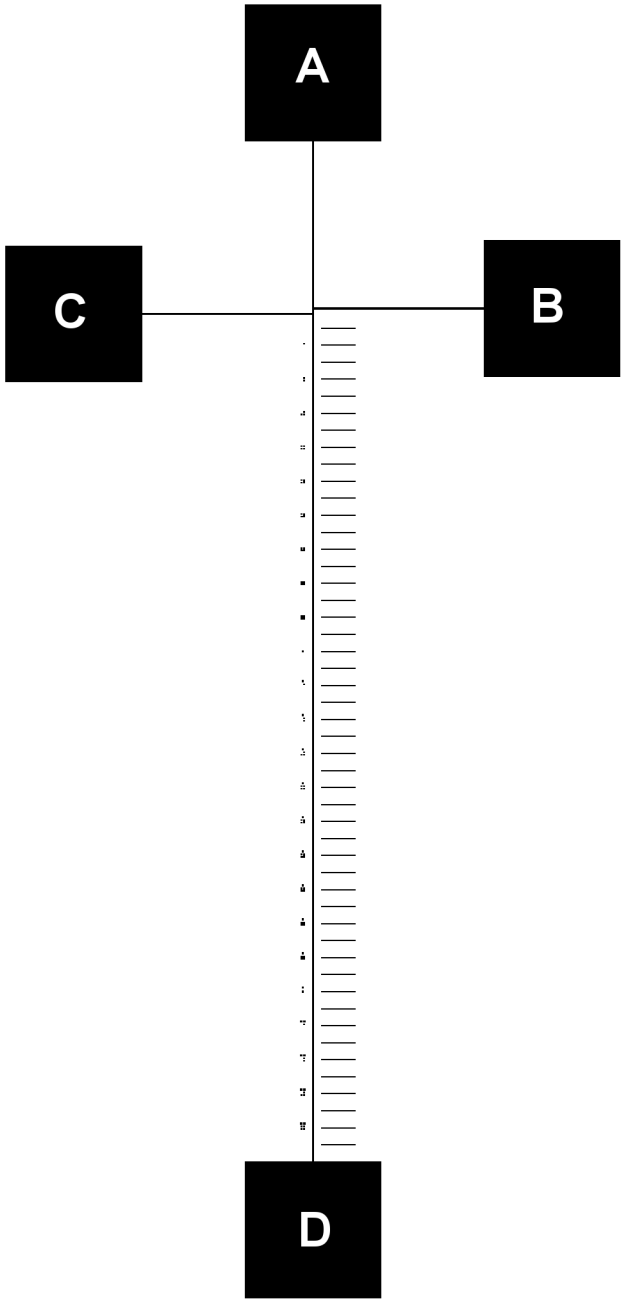

Figure 2.2: The actual channel design used for all experiments. Channel lengths of short arms were 5 mm. The separation arm is 25 mm long. All reservoirs were 5 mm $\times$ 5 mm. Along the right side of the separation channel are hash marks every 0.5 mm. These are tallied on the left using an adapted dot-dash tally.

etch proceeds for 5 minutes, with gentle agitation throughout. Following the Cr etch, the glass plate is rinsed in running DI water. After drying with filtered nitrogen, the glass plate is submerged in a buffered oxide etchant (BOE), which is hydrofluoric acid diluted 10:1 in DI water. The glass plate is left to sit in the etch bath for ≈45 minutes, which typically yields an etch depth of 20 μm. At this point, the glass plate has both photoresist and a Cr layer functioning as etch masks, although only the Cr acts as a true etch mask during the BOE etch. Original efforts removed the resist prior to etching in BOE, but I found that incomplete cleaning often resulted in photoresist residue partially masking areas of the channel, which then created roughness in the otherwise smooth walls of the finished device. After etching in BOE, the photoresist is removed through rinsing in an acetone bath. After removal of the photoresist, the Cr is removed by five minutes of agitated soaking in the Cr etchant.

With the channels etched into the glass, the plate is diced into individual devices. These devices were originally designed to fit on a glass slide, and therefore are 1" wide and 2" long. The glass is scored using a diamond-tipped stylus, then carefully fractured manually. With approximately 20 firm passes with the diamond stylus, the glass usually fractured along the desired direction. Once the devices are separated, they are placed in a bath of 1 M sodium hydroxide (NaOH) and sonicated for one hour. This procedure was a holdover from earlier processing techniques, but serves as a harsh cleaner of DNA from the glass. After sonication, the devices are rinsed with DI water and dried in an oven set to 80°C. The dried devices are then cleaned in a Pirhana solution (1:1 ratio of 96% sulfuric acid and hydrogen peroxide) heated to 100°C for one hour. Following this, they are rinsed with and then stored in DI water. This cleaning step is critical for maintaining the high wettability required of the glass during later stages. The Pirhana cleaning restores most of the surface groups to pure Si-OH bonds. The glass retains its cleanliness as long as it remains in the DI water, as tested over months of storage.

These glass devices are sealed with flat, clean PDMS lids. The PDMS used is Sylgard 184, prepared using a 100:9 ratio of elastomer base and crosslinker. In my experience, it is better for future wettability to have too little crosslinker than too much – too much crosslinker leads to a more brittle PDMS slab that is less likely to reversibly bond to the glass, and less likely to wick DI water down the microchannels. For typical use, roughly 40 g of PDMS base is used to cover a silanized silicon wafer to a depth of ≈5 mm. The PDMS is cured for >24 hours in an oven set to 80 °C. The PDMS is removed from the oven and allowed to cool immediately prior to use in bonding to the glass devices. The entire process is similarly intensive to the rapid prototyping default technique of molding PDMS with the

added benefit of creating reusable (instead of disposable) devices.

2.3 Growing Colloidal Crystals

After removing a glass device from the DI water, the PDMS is cut from the wafer, then cut along its middle in a strip ≈2" wide. This strip is then cut into three 1"-wide lids, which can be used to fabricate three total devices. A lid is selected for the device, then aligned alongside the glass device. Holes are punched through the PDMS through the side that was in contact with the wafer, to align with the reservoirs on the glass device. Placement of the holes should be slightly overlapping with the channels, and not well within the reservoirs templated on the photolithography mask. This reduces the surface area created by the air-liquid-glass interface during wetting and crystal growth, and is key to creating rapidly-grown crystals as well as better-controlled DNA injections. The PDMS is then blown clear of any debris with filtered air prior to being rinsed sequentially with ethanol and DI water. After the rinsing is complete, the PDMS slab is again blown dry with filtered air and then immediately placed into contact with the glass device.

Immediately after the device seals, which can be observed through the spreading of clear contact areas (non-contact areas, such as the reservoirs and channel, will reflect light at a shallow angle), reservoir A (Figure 2.2) is filled with 30 μl of DI water and allowed to wet the rest of the microchannels. Wetting appears similar to observations of contact: areas that once reflected light become clear when observed with indirect light. The wetting should proceed within a few seconds if all the surfaces have been properly treated. After reservoirs B and C have been wetted, 30 μl of DI water are added to them as well. The device is now prepared for addition of the colloidal suspension.

Crystal growth rate is directly proportional to the rate of colloids appearing at the growth front. This in turn is proportional to the convection speed and colloid concentration. To control the growth rate, the easiest variable to control is the concentration of the colloids. The convection speed depends largely on the evaporation rate, which requires control over the local humidity. By contrast, the relative concentration can be controlled by exploiting the three wet reservoirs. I add 30 μl of DI water to reservoir A and 30 μl of colloidal suspension to reservoirs B and C. By carefully controlling the relative heights of fluid in each reservoir, one can balance the flow rate of each source and therefore control the concentration. If reservoir A dominates, then the concentration decreases. If either of the colloid reservoirs dominate, the concentration increases. For the first set of experiments, I used a source concentration of 1% w/w of 900 nm silica colloids, such that I could have slow

enough growth to grow very ordered crystals. The second set of experiments required more uniformity, and therefore were fabricated rapidly with 10% w/w of 900 nm silica colloids.

Once the crystal has grown down the channel to within 5 mm of the desired cutoff point (usually the injection location), growth needs to be carefully monitored. To stop the growth, one needs to remove the colloidal suspension from reservoirs B and C. This is accomplished by pipetting out the reservoir and then rinsing it with fresh DI water. Usually 5-6 rinses are required before the reservoir is mostly emptied of colloids. It is helpful to "swish" the water to resuspend any colloids that may have settled during the growth period, which can last up to a few hours. It is important to begin this process in advance of the targeted crystal length, as there is usually a "lag" of 1-3 mm of growth after removal of the colloids and preparing the device for further use.

2.4 Addition of Buffer to Prepared Device

The final step in preparing the crystal-carrying device for use is the addition of running buffer. Prior to this step, the crystals can be stored with flat PDMS lids covering all four reservoirs and placed in a covered petri dish for up to a week. It is helpful to store them with reservoir A having a higher fluid level than B and C, to inhibit any further crystal growth from stray colloids. Throughout this week, the crystal that is exposed in reservoir D will slowly dry out. The longer one waits before using a device, the more careful one must be when adding buffer to reservoir D. Air bubbles introduced at this stage can remove any chance of establishing an electric connection along the separation arm, rendering the device useless.

The running buffer used is 2.5x TBE with 0.1% w/w polyvinylpyrrolidone (PVP) and 1% w/w ascorbic acid (AA), which is made of 0.22 mM tris base, 0.22 mM boric acid, and 7.1 μm EDTA (ethylenediaminetetraacetic acid). Prior to use, the buffer is pH tested. The pH needs to be higher than 8 to avoid DNA sticking to the glass surfaces. The PVP is used to reduce electroosmotic flow, which opposes the DNA direction of motion and can be high enough to prevent electrophoresis entirely. If one chooses not to use PVP, then increasing the buffer concentration to 4x can alleviate most electroosmotic flow concerns at the cost of decreased time to salt out, which causes the experiment to end and will be discussed below. The AA is used as an oxygen scavenger, which helps to reduce photobleaching of the intercalating dye used to stain the DNA molecules for fluorescence detection.

Adding the buffer is first done by removing all DI water in each reservoir and adding 60 μl of buffer to reservoirs A, B, and C. The device is then left to sit for 15 minutes as the

evaporative flow helps to drive the buffer through the microchannels. After 15-20 minutes of such flow, 60 μl of buffer is added to reservoir D slowly, with careful observation through the microscope to avoid trapping air within the end of the crystal. After adding to D, another 15 minutes of equilibrating is done to allow the fluid levels in the reservoirs to level out. This step is best carried out with the device slightly covered from the ambient air to slow evaporation. If desired, prior to covering the device, one can insert the platinum electrodes into the reservoirs to allow time for the fluid levels to accomodate the volume of the added electrodes.

2.5 Choice of DNA Sizes and Their Preparation

All of the DNA used in the following studies is dyed with YOYO-1 intercalating dye from Invitrogen and stored in 2.5x TBE buffer with no additives. The YOYO-1 molecule only binds to the backbone of double-stranded DNA, and is therefore especially useful in cases where there may be a mixture of DNA and polymerase chain reaction (PCR) reactants (PCR uses unbound nucleotides as the building blocks during polymeration of new DNA strands, but not all of these nucleotides are consumed during PCR). In general, we use a 5:1 bp:YOYO-1 ratio designed for maximal fluorescence intensity. This is done by estimating the DNA mass in μg, then using 0.308 μl of stock YOYO-1 for each μg of DNA present. Initial separation studies were done using a PCR marker purchased from New England Biolabs, which contains the following fragments: 50, 150, 300, 500 and 750 bp. These were found to be separable in 900 nm colloids within an elution distance of 15 mm for electric fields ranging from 15 to 40 V/cm. Therefore, the experiments using small DNA were done using two DNA molecules with molecular weights on either end of the PCR ladder.

To create these DNA, I chose to go through a process of PCR cloning of small reads from the pNEB193 plasmid, purchased from New England Biolabs. The PCR process uses short, single-stranded DNA primers as templates for copying selected strands of the DNA. The standard PCR process for 50 μl of product requires a specific mixture of ingredients: 5 μl each of the left and right primers (10 μM), 1 μl of DNA template (5 ng/ml), 14 μl of DI water, and 25 μl of TAQ 2X Master Mix solution of nucleotides and buffer (New England Biolabs). This mixture is then cycled through a range of temperatures designed to open the DNA template, polymerize from one primer to the second primer, then release. On the next cycle this process repeats, including the new products. The result is an exponentially increasing number of copies of the template DNA with a number of basepairs equal to the distance between the ends of the two primers. The primers are 20 bp sequences chose with

the help of the Primer3 website, which selects primers designed to yield successful PCR products within a specified size range. The sizes chosen for the first tests were designed to be 86 bp and 709 bp in length.

An individual PCR reaction will typically yield concentrations of ≈1 μg/ml of DNA. For facile fluorescence measurements in these devices, concentrations of at least 10 μg/ml are required. Therefore, many of these PCR reactions needed to be combined and concentrated prior to use. To accomplish this I would run a full batch of PCR reactions, which is 25 tubes $\times$ 50 μl. I used two tubes, selected at random, to be run in an agarose gel to confirm correct amplification of the DNA. Another two vials would be selected for purification in Qiagen MinElute columns. These columns are designed to wash off PCR reactants, leaving behind only the double-stranded products. After resolubalizing the MinElute products, I was able to check their concentration in a NanoDrop 2000c UV-Vis Photospectrometer, which measures the absorbance of the nucleotides present (necessitating the reactant cleanup). This provided me with an estimate of the concentration of DNA in each PCR tube. The remaining PCR tubes are combined and concentrated using the standard ethanol precipitation method. This method preserves all of the nucleotide materials, and therefore does not remove all of the PCR reactants. However, the yield of the ethanol precipitation method is similar to that of the MinElute columns (≈80% efficiency), which allows for simple estimation of the amount of PCR product created. A typical batch, following concentration and dying, yields ≈50 μg/ml of DNA.

The λ-DNA used in the second study was taken from stock solutions of 500 μg/ml, while we used the full PCR Marker (a mixture of 750, 500, 300, 150 and 50 bp fragments at a total concentration of 500 μg/ml), both purchased from New England Biolabs. They were also dyed with YOYO-1 using the same procedure as other DNA, using instead a dye ratio of 0.2 μl YOYO-1 per μg of DNA. The target concentrations for the λ-DNA were also ≈150 μg/ml. In any mixtures of different sizes, it is important to balance the mass concentration of each size, since the same molar amount of short DNA will have less fluorescence/molecule than larger DNA. This is especially important when combining the λ-DNA with the PCR ladder, which was also dyed with the lower concentration of YOYO-1.

2.6 Controlling Electrophoresis Experiments

Our actual electrophoresis experiments are controlled through a custom LabView program that controls the PriorScan stage, LabSmith HVS power supply, and collects the stage position and fluorescent intensity data from the photomultiplier tube (PMT). The chip is

carefully mounted into the PriorScan stage, then covered with a custom-made electrode holder. The electrode holder fixes the power supply cables at the point where they join copper wires, which are the flexible mounts for the platinum electrodes inserted into the reservoirs. After equilibrating, the stabilized device is pre-run with a voltage drop from the A reservoir to the D reservoir of 200 V, the same direction as the initial loading step for a shifted-T injection. This helps to stabilize the crystal against future field-induced de-aggregation. Running the voltage drop the opposite direction (D to A) usually results in the colloids nearest the injection position decrystallizing and flowing towards the injection. After this has occured, the crystal is ruined and no longer worth pursuing, as the crystal will not have a flat crystal interface and any band of injected DNA will be catastrophically broadened in the crystal entrance.

The LabSmith power supply is capable of setting the potential of each electrode relative to a common ground, which is connected to the microscope base. To calculate the desired voltage for each potential, we assume that the shift in the shifted-T is negligible, and the device can be modeled as four wires with a common junction. The resistance of each wire, if only filled with buffer, will be linearly proportional to the length ($R = \rho L/A$), where ρ is the resistivity of the buffer, L the channel length, and A the channel area. When constrained with Kirkhoff's law for conserving current, this results in a straightforward calculation for the potential of each of the arms: set a "ground" reservoir, choosing the electric fields desired for each arm, calculating the junction voltage, then determining the necessary ΔV to get the desired E.

However, the process is less straightforward when the area A of channel D is not constant. This occurs because the cross-section is partially packed with colloids, which have a packing fraction of 0.74. The result is that part of the total length of D is a resistor whose resistance is modeled by $R_c = \rho L_c/A_c$, where A_c is the effective cross-section available for ionic conduction. To set an electric field E_d that is valid across the higher-resistance crystal section, we use an effective length, L_{eff}, which results algebraically from solving the problem described above:

$$L_{\text{eff}} = L\left(1 + f\left(\frac{L_x}{L} - 1\right)\right) \tag{2.1}$$

This resistance assumption was experimentally determined to have a "packing fraction" $f = 0.79$, which I believe represents some of the double-layer effects present with the large amount of charged surfaces (see Figure 2.3). The experiment was performed by measuring the resistance of crystals of various lengths, plotted as a fraction of the total length vs. the resistance of the crystal. Fitting with the equation described in Figure 2.3 yielded the fitted

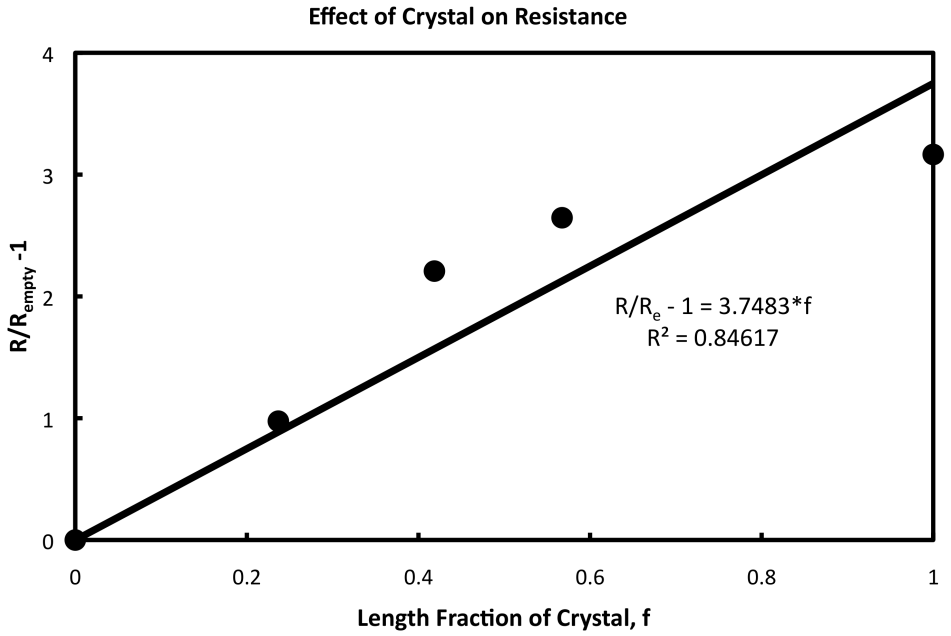

Figure 2.3: Verification of close-packing through measuring the resistance vs. length fraction of packed channel. Assume a total resistance $R = R_x + R_e$, where R_x is the resistance of the crystal and R_e the resistance of an empty channel. R_e is given by $R_e = \rho L_e/A$, where ρ is the resistivity of the buffer, L_e is the length of empty channel, and A the channel cross-sectional area. Therefore, $R_x = \rho L_x/\left(A\left(1-\phi\right)\right)$, where L_x is the length of crystal in the channel and ϕ represents the packing fraction of colloids, which reduce the effective cross-sectional area. If $f = L_x/\left(L_x + L_e\right)$, then we can see that $R/R_e - 1 = f\left(1/\left(1-\phi\right) - 1\right)$. Using the data obtained in Figure 2.3, we find $\phi = 0.79$, or a packing fraction of 0.79. The value is used in all later calculations accommodating the crystal.

packing fraction, which was used in the LabView program when setting the electric fields.

After the current stabilizes during the pre-running, the pre-running fields are turned off and 30-40 μl of buffer are removed from the B reservoir and replaced with an equivalent amount of DNA solution. The LabView program then loads DNA using a high electric field drop between reservoirs B and C (140 V/cm) and "pinching" negative fields from channels A and D of ≈-30 V/cm. The device is loaded for 30-60 minutes to allow for stabilization of the DNA. Larger DNA molecules such as λ-DNA can take a long time to migrate through the low electric fields in the reservoir to the channel entrance, which is required for maximum concentration prior to injection.

The injection fields used are typically 70 V/cm towards reservoirs B and C, 60 V/cm towards D, and the balance pushing from A to satisfy Kirchoff's Law at the junction point. High injection fields are used to ensure a tight injection band, sometimes called an injection "plug." Then, sometime before the plug reaches the crystal, the injection field is switched

to the separation field, which is usually in the 10-50 V/cm range towards D. The field in reservoirs B and C is kept the same to prevent DNA "leaking" back into the separation channel.

The LabView software is designed to perform "scanning mode electrophoresis" [29]. A "scan" consists of measuring DNA fluorescence intensity as a function of position in the channel. This is very similar to the snapshots taken of an agarose gel following a separation. One can measure the distance travelled in a set amount of time under a set electric field. In the LabView software, the program moves the stage along the separation channel, measuring the fluorescence intensity as a function of position (see Figure 2.4). The stage moves at 7 mm/s, and so is able to transit the entire 25 mm separation length in seconds. The fluorescence data is collected by a photomultiplier tube (PMT), which collects data as a voltage from 0-10 V. The gain on the PMT can be increased for weak signals at the cost of also amplifying the noise of the measurement. The LabView software has built-in noise-reduction high-pass filter which removes data above 100 Hz, and which can be toggled off to increase the amount of data collected.

After the experiment is concluded, the data collection files can be closed by stopping collection in the LabView software. After changing the output filename, one can then start to reload DNA and make a second injection. The second loading phase generally takes less time than the first, usually only 20 minutes. The user can also change the separation fields or loading fields prior to making a second separation. This process can be repeated for as long as the device continues to function, which will be discussed in the last section. After concluding the experiments for the device, the entire LabView program is stopped and the power supply is turned off. The device is removed and the PDMS and liquid wastes are rinsed into a hazardous disposal container designated for YOYO-1 toxins. The glass is rinsed and placed in a 1 M NaOH bath to be prepared for eventual reuse.

2.7 Failure Mechanisms

Along the process of fabricating the crystals for electrophoresis and their use in separations, there are a few typical failure routes that can occur. They are outlined below with a brief explanation as to their probable cause, and routes towards minimizing their reoccurrence in the future.

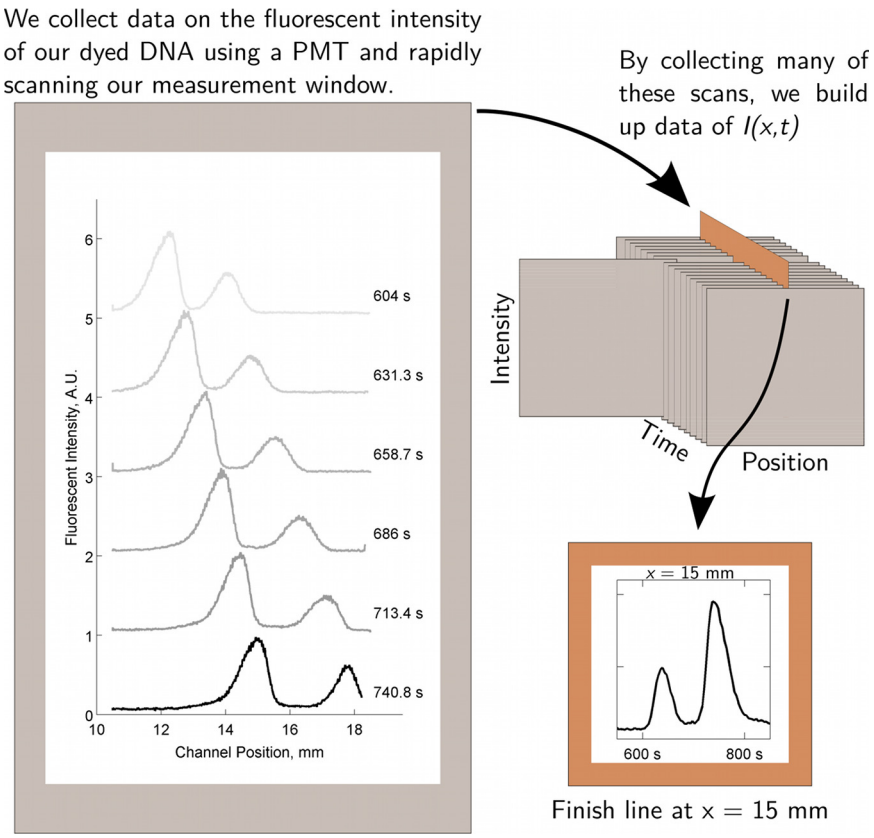

Figure 2.4: Scanning mode electrophoresis can be used to generate finish line data if scans are taken in rapid succession. The first set of experiments uses finish line data, while the second set uses the scans. Each tool can be used to answer different questions, however with high density scanning the choice between tools can be made after the experiment is concluded.

2.7.1 Problems with initial wetting

During the initial wetting step immediately after mating the PDMS and glass surfaces, two problems may occur related to wetting. The first is that the DI water does not spontaneously wet the entire device. This is usually a result of either imperfect cleaning, or PDMS with too much crosslinking. In these cases, one should scratch a an identification mark on the back of the glass device and then submit it for cleaning again. If the same device has trouble wetting, it may have accumulated too much wear throughout its life and should be discarded.

The other problem occurs when one adds water to the B and C reservoirs before they have been completely wetted from A. In that case, a bubble of air may be trapped at the entrance of either the B or C channels. These bubbles prevent any fluid connections and will likely inhibit any further use of the device. They are nearly impossible to remove, but

some success may be achieved by removing all of the liquid from the offending reservoirs and waiting for them to dry out, and the initial wetting process to continue. However, it is generally more expedient to start over with a fresh glass device and PDMS lid.

2.7.2 Crystal comes apart during prerunning

In some cases, poorly packed crystals can be broken up after applying the electric field. This damage is generally irreversible, although it may appear to be fixed by reversing the electric field direction. This is because the fundamental packing has been disturbed, and a future failure route established. If this occurs, it is best to discontinue service on that device and prepare a second device for testing. It will also spare the consumption of any DNA.

This generally happens when the crystal has not had ample time to equilibrate following crystallization. Best results come from equilibrating the recently grown crystal overnight at a minimum, although it can be done in as little as an hour after initial crystallization. The crystal may also come apart on rare occasion during the actual electrophoresis, in which case it is usually noted after the elution has progressed. In these cases, it is best to retain the data with a note to watch for any anomalous behavior. This will usually manifest in DNA bands that appear to slow down or stop in the middle of an elution.

2.7.3 DNA injection issues

This is usually noticed after the researcher has left the DNA to inject for 30 minutes, and arrives to find no DNA has entered the device or that DNA has spilled into the A or D channels. This is generally caused by one of two factors. The first is a lack of electrical connection, implying an incomplete fluid path from electrode to electrode. In cases where there is no injection, it implies that the electrode in the C or B reservoirs is either out of the reservoir, or an air bubble has cut off the electrical connection. In cases where the DNA has spilled into the side channels, the same culprit may be at hand. The alternative problem is a bulk flow problem, where the fluid reservoir heights are mismatched and the fluid is flowing either with or against the DNA, depending on the symptoms. This can be corrected by careful addition and subtraction of fluid from the suspect reservoirs. It is generally easiest to attempt to lower the source reservoir, but care must be taken to not cause flow in other directions. Inability to control the DNA injection will prevent the use of the device for any separations, but is not a guaranteed failure of the device.

2.7.4 Reservoirs dry out

Throughout the typical four hours of running, the fluid in the reservoirs will continue to evaporate. In extreme cases, the fluid level may drop significantly enough to break contact with a shallowly-placed electrode. In these cases, one can either lower the position of the electrode or add back buffer to the reservoir. When the choice is made to add fluid, it is critical to add an equivalent amount of fluid to each reservoir to avoid generating any hydrostatic pressure flows. It is also important not to do this during an elution, as it has the potential to alter the flow of the device and could interrupt an ongoing separation.

2.7.5 DNA stops during an elution

In cases where the DNA appears to stop in the crystal, there are generally two culprits. If the DNA stops near the entrance of the crystal, this is generally indicative of the DNA adsorbing on the colloids. This is caused by having a buffer pH < 8, and cannot be remedied without starting over. In these cases, the buffer stock should be immediately remade to avoid future complications.

If the DNA stops later in the run, it may be caused by salting out of the buffer. The PDMS used as a lid is water-permeable, and thus is also a source of evaporation during the total elution time. If the water content of the buffer drops too low, the buffer will begin to precipitate salt crystals. At a critical concentration, the salt crystals will grow large enough to block the entire channel cross-section, breaking the fluid electronic circuit. In these cases, the DNA will stop as it no longer feels any potential drop. These salted out regions can be discovered using light microscopy, as they will usually have the index of refraction similar to the glass and the colloids. Areas where it would be easy to identify the crystal before will appear clear and empty – implying a salt matrix around the colloids there. In these cases, one should note how long they were able to run their device, and plan accordingly for future runs. This will occur faster in higher TBE concentrations, which is part of the reason PVP is used to mitigate EOF instead of increased buffer concentration.

2.8 Methods Summary

The methods described above were used for all following experiments, with deviations noted as they are made. This process was used to create glass devices lasting years of reuse with little ill effects. As a prototyping process, the use of glass as a stable structure aided iterative testing. Using removable PDMS lids helped to clean out the devices and reset them for future use, removing the time- and material-intensive glass fabrication from the

researcher's consideration. This process was refined prior to obtaining any of the results presented in this thesis, and therefore has enabled straightforward comparison of all data obtained thereafter.

Chapter 3

Crystal Quality and its Effects on Separations

This chapter is based on the publication:
King, S.B. and Dorfman, K.D. Role of order during Ogston sieving of DNA in colloidal crystals. *Anal. Chem.* **85**(16):7769–7776, 2013.

3.1 Summary

We combine *in situ* Bragg diffraction, laser diffraction, high speed fluorescence scanning, and large-scale data processing to arrive at statistically significant conclusions about the role of order during the microchip electrophoresis separation of short DNA molecules (86 basepairs and 709 base pairs) in colloidal crystals. This experimental approach directly connects the presence of long-range order (obtained by laser diffraction) to the DNA transport (obtained by fluorescence detection) in hundreds of "mini-columns" comprised of 500 μm-long regions of the devices. To within statistical significance, the electrophoretic mobility is the same in regions of the chip with long-range order and those with short-range order, independent of the electric field and molecular weight. Moreover, the relative mobilities of the DNA agree well with a recent estimate for the Ogston sieving mobility in a colloidal crystal. Similar to previous work, the band broadening during the transit through the colloidal crystal is negligible. These features imply that colloidal crystals for DNA separation in the Ogston sieving regime do not require exquisite control over the microstructure to maximize the separation resolution, simplifying their assembly for routine use.

3.2 Introduction

The key to understanding (and thus optimizing) DNA separations is connecting the detailed microstructure of the separation medium to the DNA dynamics therein. At one extreme, transport in disordered media such as agarose and polyacrylamide gels is ubiquitously described by mean-field approaches to characterize the medium [4] that rely on the average pore size or a statistical model of the pore size distribution [30]. At the other extreme, we can exactly describe the pore sizes and connectivity in two-dimensional microfabricated DNA electrophoresis devices, simplifying the models for the transport phenomena therein [31]. DNA electrophoresis in colloidal crystals [8, 9, 11, 18, 19, 21, 22] is a fascinating and relatively unexplored intermediate case between a gel and a microfabricated system. Colloidal crystals formed from monodisperse, micron-sized spheres provide a three-dimensional separation matrix, similar to an agarose gel, but the local ordering of the pores is closer to a microfabricated system. The colloidal crystals used for DNA separations [9] are grown *in situ* by a method known as convective self-assembly (CSA) [5]. While crystalline regions spanning many particle diameters can be fabricated with CSA by carefully controlling the processing [5, 6, 25, 27, 32, 33], the column lengths required for DNA separations normally span thousands of colloid diameters. Moreover, the channel walls can lead to boundary-induced defects that result in a loss of ordering in the crystal [6]. Under these conditions, the colloids may be ordered over tens or hundreds of colloid diameters, but the overall column morphology is polycrystalline, with a random close-packed configuration of many small grains. In the present contribution, we use a combination of materials characterization and DNA transport measurements to show that long-range crystalline order is not important for separating short DNA in the Ogston sieving regime. While large, single-crystal regions are critical for other applications of colloidal crystals, such as in photonics [34, 35], our results indicate that growing large crystals for DNA electrophoresis is superfluous.

Proof-of-principle experiments indicate that colloidal crystals perform well as molecular sieves for a wide range of DNA sizes when integrated into microfluidic electrophoresis devices [8, 9, 18, 19, 21]. However, the connection between the microstructure and the separation performance is not as well established. To date, only two studies have touched upon the role of crystalline order on DNA electrophoresis in colloidal crystals. The pioneering experiments by Meistermann and Tinland [8] used laser diffraction to characterize the medium, providing volumetric structural information in the wet crystal. While their materials characterization indicated the presence of regions with and without long-range ordering, they did not report any data as a function of the crystalline order. More recently, Harrison and coworkers [19] investigated DNA prism separations [36] in a bidisperse mixture of two disparate colloid

diameters. As expected, the presence of small and large colloids in the matrix leads to a distribution of pore sizes. The best separation resolution occured in crystals formed from monodisperse colloids, since the band broadening came almost entirely from the pore size distribution [19]. While the latter study highlighted the need to avoid gross distortions of the crystalline lattice produced by doping with a large colloid, it did not address the more subtle question of polycrystallinity and the concomitant variations in crystalline order that are still present in monodisperse systems.

Understanding the role of grain size and grain orientation on DNA separations requires (i) appropriate characterization of the length scale for ordering throughout the volume of the crystal under separation conditions and (ii) sufficient data to arrive at statistically meaningful conclusions. To address the first point, we use laser diffraction, following the original work by Meistermann and Tinland [8]. Laser diffraction, used frequently in the materials community to characterize colloidal crystals [37], probes the entire volume of crystal in the beam spot. Moreover, laser diffraction can be performed *in situ*, allowing us to characterize the presence or absence of long-range ordering over the length scale of a 160 μm beam spot size. We prefer the laser diffraction approach to the alternate method [9, 19, 21, 22] of drying out the crystal, removing the channel lid, and then imaging with scanning electron microscopy (SEM). In addition to imaging artifacts arising from drying-induced cracks [32], the key limitation of SEM is that it only images the surface of the crystal. Colloidal crystals used for separations are tens of layers deep. Confocal microscopy experiments [27] demonstrate that, for crystals that are more than 6 layers deep, stacking faults are less likely to be near the substrate. Thus, SEM images of the crystal surface may not be representative of the environment experienced by the DNA. Moreover, defects in the interior of the crystal can profoundly affect the separation resolution. For example, consider DNA electrophoresis experiments in a cubic gel phase of the pluronic copolymer F127 [38], which can exhibit grain boundaries that are similar to those found in the interior of colloidal crystals. Experiments demonstrate that migration along the grain boundaries strongly affects the electrophoretic mobility [39]. If the characterization method does not probe the interior of the crystal, it becomes challenging to connect the material characterization to the separation process.

To acquire sufficient data to make statistically significant conclusions, we use the "mini-column" approach illustrated in Figure 3.1. The initial section ($\approx$10 mm) of the colloidal crystal separates two DNA species with sufficient resolution to enable facile measurement of each peak without need for deconvolution (and the concomitant experimental error). The next $\approx$8 mm of the column is then conceptually divided into 0.5 mm long mini-columns.

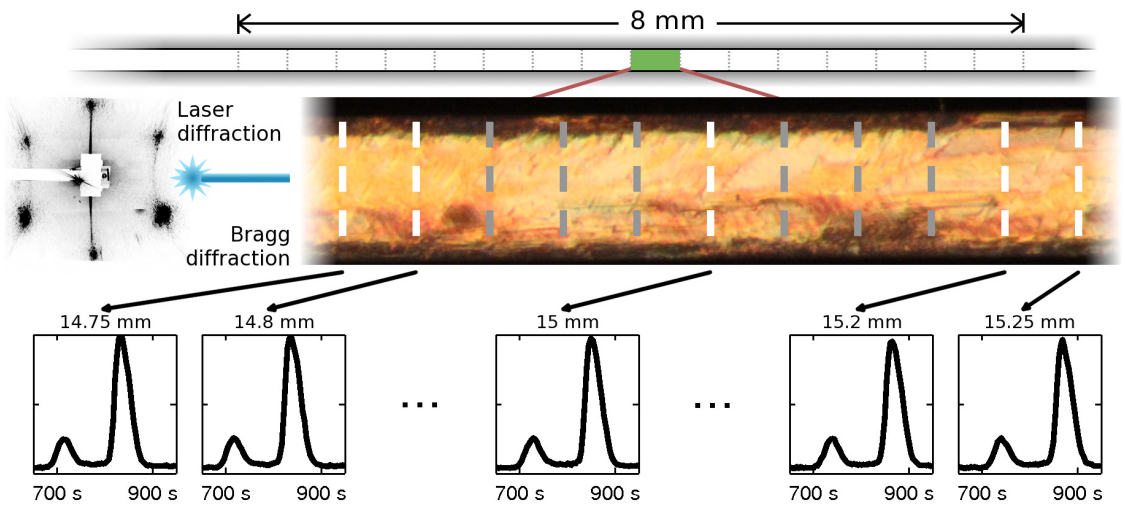

Figure 3.1: Overview of the "mini-column" approach to data collection. The separation channel contains at least 18 mm of colloidal crystal. The characterization and imaging are performed starting around 10-14 mm downstream from the injection point. In each 0.5 mm section of the column, indicated by the dashed vertical lines in the first row of the figure, we acquire a Bragg (white light) diffraction image and a laser diffraction pattern. The second row of the figure illustrates one such image and the corresponding diffraction pattern; the well defined diffraction spots indicate that this particular region possesses long-range order. The third row of the figure shows the finish-line electropherograms at the corresponding locations indicated by the dashed lines in the Bragg diffraction image.

Prior to any electrophoresis experiments, we combine optical images of the Bragg scattering of white light with laser diffraction results to qualify the orientational order within each mini-column as long range or short range. Long-range order yields bright diffraction spots over the 160 μm beam spot size, while short-range order gives us a diffuse ring at the same diffraction angle. Rapidly scanning the channel to measure the fluorescence intensity as a function of position and time during the separation allows us to create distinct finish-line elution measurements spaced 50 μm apart, yielding up to 10 unique electropherograms for every mini-column. In this way, we can ascertain both the mobility and the rate of band broadening for each mini-column. This combination of *in situ* characterization and our densely packed elution profiles yields large data sets with minimal experimental overhead; each experiment in a given chip yields 16 mini-column measurements of mobility and band broadening, along with the corresponding 16 structural characterizations. We report results from 21 such experiments in 7 different chips, using a range of electric fields, thereby analyzing more than 3000 finish-line electropherograms. The size of this data set allows us to make statistically significant conclusions about the importance (or lack thereof) of local

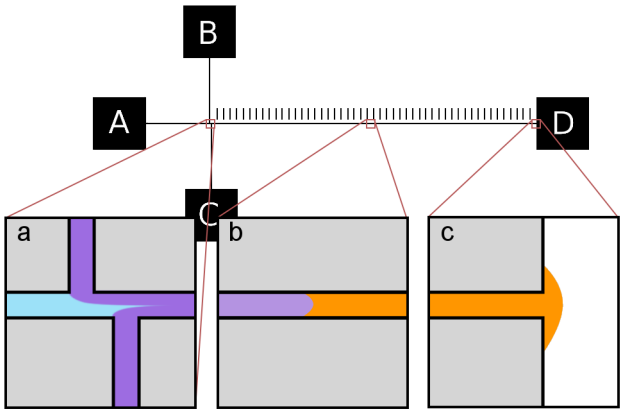

Figure 3.2: Mask for the microfluidic shifted-T channel. The fluid reservoirs are labelled with letters for future reference. The separation channel has ruler markers every 0.5 mm along its 25 mm length. The other arms are each 5 mm long, and the offset of the shifted-T is 100 μm. The insets schematically depict the convective assembly of the colloidal crystal. Inset (a) shows the colloid suspension moving from B and C towards D, mixing with the DI water from A. Inset (b) shows the growth interface as the colloidal crystal is grown. Inset (c) points out the initial seed condition required for rapid crystal growth; the crystal needs to penetrate the reservoir only slightly. The initial crystallization conditions will determine the average grain size at the onset of crystal growth, acting as a seed crystal.

ordering in the crystal on the electrophoretic mobility and band broadening.

3.3 Materials and Methods

Our microfluidic devices are fabricated in soda-lime glass via standard wet etch procedures with chrome as an etch mask. The glass channels are sealed with a PDMS lid containing punched-out holes that act as fluid reservoirs. We grow our colloidal crystals within the device as shown in Figure 3.2 using 900 nm diameter silica colloids (Bangs Labs) using standard convective self-assembly [9]. The crystal growth rate is controlled by modifying the relative concentration of colloids in the separation arm (see Figure 3.2) with the purpose of creating distinct regions of long-range and short-range order. Once the crystal growth interface nears the shifted-T injection, we terminate growth by replacing the colloid solution in the reservoirs with DI (deionized) water [9].

To qualify the heterogeneous order, we use laser diffraction. Our laser diffraction apparatus consists of a stage, mounted on two micropositioners (Thor Labs) that allows us to scan through the channel, and a 135.95 mW, 473 nm blue laser (Laserglow.com) beam normal to the chip. We use a lens to focus the laser to a spot size of roughly 160 μm on

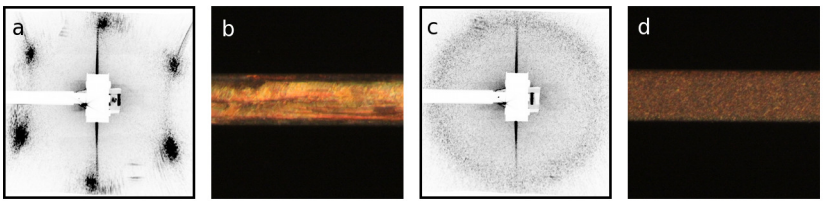

Figure 3.3: Example of a mini-column with long-range/short-range ordering illustrated by (a/c) laser diffraction and (b/d) white light Bragg diffraction. The diffraction pattern measures the orientational order of the entire volume of the crystal within the 160 μm-wide beam spot at the center of the mini-column. It is important to note that the diffraction patterns in (a) and (c) occur at the same distance from the undiffracted beam in the center, demonstrating that they have the same diffraction angle and therefore the same nearest-neighbor distance under both ordering conditions.

the colloidal crystal inside the channel, which then diffracts onto a screen 10 cm behind the chip. This diffraction pattern is recorded by a 12-bit monochrome CCD camera (QIClick) with a 25 mm fixed focal length lens (Edmund Optics) located 60 cm further along the axis of the beam. We use a beam stop to protect the CCD from the undiffracted beam. We only capture the first-order diffraction peaks, which are sufficient to classify the long-range ordering of each mini-column.

In order to make reliably spaced diffraction measurements every 0.5 mm along the channel, the mask design includes regularly spaced 50 μm wide, 500 μm long ruler markers next to the channel edge. After the device fabrication, these lines lead to small, air-filled cavities that also diffract the laser light. To make the diffraction measurement for a given mini-column, we first align the laser on the corresponding ruler marker, and then measure the diffraction in the channel immediately below that marker. By repeating this procedure along the entire channel length, we obtain the laser diffraction data throughout the channel in a manner that allows us to directly connect the diffraction data to the transport data.

In addition to the laser diffraction pattern, we also record the white light Bragg diffraction pattern at each mini-column position using an inverted microscope (Leica DMI-4000), a commercial camera (Canon EOS Rebel T1i 500D) and a 10x Leica objective. We use a compact fluorescent lightbulb in a desk lamp as a light source. The latter images are easily aligned with the laser diffraction measurements through the ruler markers in the channel design.

If a mini-column possesses long-range ordering, it will exhibit the distinct diffraction peaks seen in Figure 3.3a. The spots are the typical diffraction pattern of a mixed close-packed crystal containing both hexagonal close packed (HCP) and face-centered cubic

(FCC) layer packings — generally occurring in hexagonal patterns for the first-order diffraction pattern. It is also possible to have a small number of dominant orientations, which leads to multiple six-fold patterns oriented at different rotational angles at the same diffraction angle. Conversely, mini-columns with short-range ordering produce the rings seen in Figure 3.3c. The nearest-neighbor spacing in these is the same as in Figure 3.3a. The ring implies the presence of many different crystal orientations, which tells us the section being measured has many different grain orientations and therefore many small grains (much smaller than the $\approx$160 μm beam width). In previous DNA separation work in colloidal crystals, white light Bragg diffraction alone was used as an indicator of a close-packed crystal *in situ* [9, 18, 19, 22, 23]. Figure 3.3 shows that crystalline regions with both long-range order and short-range order both exhibit Bragg diffraction of white light. However, a crystal with long-range order will have significantly more coherent and strong diffraction as indicated in Figure 3.3b, a distinction not noted in the previous work [9,18,19,22,23]. Thus, it is possible to use the intensity of the white light Bragg scattering to make a cursory qualification of the crystallinity without resorting to laser diffraction, but the presence of white light Bragg diffraction does not imply long-range order.

For our experiments, we used PCR amplicons of 709 and 86 basepairs (bp) in length obtained from the pNEB193 plasmid (New England Biolabs). After amplification and purification, they are dyed with YOYO-1 intercalating fluorescent dye (Invitrogen) and kept in a 2.5x TBE buffer (Tris base, boric acid, and EDTA) at concentrations ranging from 10-70 μg/mL. Immediately prior to separation, they are mixed in an approximate 1:2 volume ratio (709 bp:86 bp) in an effort to balance their fluorescent signals by balancing their relative concentrations. The running buffer is the same 2.5x TBE with 0.07% polyvinyl pyrrolidone (Sigma Aldrich) and 0.07% ascorbic acid (Fisher-Scientific).

The DNA used for these experiments are PCR amplicons of segments 709 and 86 basepairs (bp) in length obtained from the pNEB193 plasmid (New England Biolabs) using the primers [5'-TATCCGCTCACAATTCCACA-3' and 5'-AGTCGTGTCTTACCGGGTTG-3'] (709 bp) and [5'-GTCTTGAGTCCAACCCGGTA-3' and 5'-GCCTACATACCTCGCTCTGC-3'] (86 bp) (Integrated DNA Technologies) and Taq 2X Master Mix polymerase (New England Biolabs). Successful PCR amplification is confirmed by agarose gel electrophoresis. Following PCR, these amplicons are concentrated and purified by ethanol precipitation. The DNA are dyed with the intercalating fluorescent dye YOYO-1 (Invitrogen) at a dye-to-basepair ratio of 1:5 by rocking overnight. The DNA are kept in 2.5x TBE buffer (Tris base, boric acid, and EDTA) and stored unmixed at concentrations between 10-70 μg/mL. This concentration is estimated by filtering two of the 25 PCR tubes of each

batch through the Qiagen MinElute PCR purification kit and assuming the efficiency of the elution column and ethanol precipitation are similar. The concentration of the filtered DNA is calculated by measuring the absorbance of 260 nm light using a Nanodrop 2000c Spectrophotometer (Thermo Fisher Scientific). A similar measurement of the precipitated DNA gives erroneously high results, as the unbound nucleotides of the PCR mixture are not removed yet absorb at the measurement wavelength, registering a very high concentration (thousands of mg/mL). We choose the precipitation method because it allows us to reach higher stock concentrations than the Qiagen kits.

These precipitated and dyed DNA are mixed immediately prior to loading into the device, in ratios that should balance the total intensity of each injected peak. This typically requires 1 part of the 709 bp solution and 2 parts of the 86 bp solution. Since the stock concentration values are only estimates, the actual peak intensities are not exactly in balance (see Figure 3.1). For our separation measurements, the relative concentrations are more important than the absolute concentrations, as equal peaks are more easily deconvolved during full-width at half-maximum measurements.

One hour prior to performing the electrophoresis experiments, we replace the DI water in all reservoirs with 60-80 μL of 2.5x TBE supplemented with 0.07% polyvinyl pyrrolidone (Sigma Aldrich) and 0.07% ascorbic acid (Fisher-Scientific). After allowing the pressures to equilibrate for 15 minutes, platinum electrodes are inserted into each of the reservoirs and the device is pre-run for 45 minutes at $\approx$20 V/cm in the separation arm to stabilize the crystal, similar to previous work [9]. For our electrophoresis experiments, we use a LabSmith HVS448-1500 high-voltage power supply to control the potential in each of the four reservoirs. The potentials are calculated in our custom LabView controller by treating the device as four conductors of resistivity ρ, fluid cross-sectional area A available for conduction, and length L, with a shared junction and conserving current. We also take care to account for the non-uniform resistivity of the crystal in the separation arm by treating that "wire" as two resistors in series, where the resistance of each section of the wire, $R_i = \rho L_i/A_i$, accounts for both its length and the cross-sectional area available for conduction through the fluid. After 45 minutes of pre-running, the electric fields are turned off and the DNA solution is loaded by first removing 30 μL of running buffer from reservoir B and replacing it with 30 μL of dyed DNA solution. The DNA are loaded using the standard shifted-T protocol [40], and the typical injection width is $\approx$100 μm.

Our electrophoresis experiments are performed using a custom LabView program to control a LabSmith HVS448-1500 high-voltage power supply, thereby controlling the potentials in each reservoir. The applied potentials are calculated within LabView by treating

each of the four arms of the device as wires with resistance $R = \rho L/A_0$ proportional to their length, L, with an identical ionic resistivity, ρ, and cross-sectional area, A_0. In the case of the separation arm, we account for the crystal by treating that "wire" as two resistors in series. The resistance of the empty length is treated the same as the other empty arms, while we treat the crystal of length L_c as having lowered the available area for conduction by the adjusted packing fraction; i.e. $R_c = \rho L_c/(0.79A_0)$ (see Figure 2.3). The reported electric fields are the values inside the crystal "wire", not the full length of the separation arm. We inject bands of the mixed DNA using the standard shifted-T protocol [40]. We measure the progress of our separation using a high-speed scanning electrophoresis technique adapted from the gel-based method developed by Ugaz and coworkers [29]. The fluorescence intensity is measured by translating the microscope stage (Prior OptiScan II) of an inverted epifluorescence microscope (Leica DMI-4000), using a 40x objective (NA = 0.50) to focus the emitted light onto a photomultiplier tube (PMT) (Hamamatsu H7422-40). The electric fields, stage motion, and data acquisition are automated using our LabView routine. The scanning region is the 8 mm section indicated in Figure 3.1, and the stage moves near its maximum translational speed of 8 mm/s. With the additional overhead for the LabView program and data output to disk, we obtain one scan every 4 seconds. During a given scan, the fluorescence data are acquired at 1 kHz.

The output from the electrophoresis measurements consists of a list of stage locations as a function of time and a list of fluorescence intensity versus time. Since these outputs are asynchronous and obtained at different acquisition rates, owing to differences in the hardware, we have a Python script that merges the two files into a single file of fluorescence intensity versus position and time, $I(x,t)$. Since the fluorescence intensity data are acquired at a higher rate than the stage position data, we assume a constant stage velocity between points to interpolate position data. We break the complete $I(x,t)$ file into subfiles for each forward scan. To create effective finish-line data from the $I(x,t)$ data, we pick equally spaced points at $x_{i+1} = x_i + 50$ μm, with the value $x_0 = 0$ equivalent to the center of the shifted-T injection. When those points are within our measurement window (see Table 3.1 for the measurement window locations for each device tested), we go through each scanning electropherogram file and measure the average intensity within a window of positions $x_i \pm 25$ μm. We have an automated MatLab script that automatically generates the $\approx$160 finish-line electropherograms for a given experiment from the $I(x,t)$ data.

Figure 3.4 illustrates the method of parsing the data into mini-columns. The mini-columns correspond to the regions ± 250 μm away from the center markers. Within each mini-column, we have (i) the laser diffraction pattern, (ii) the white light Bragg diffraction

Chip	Rings	Spots	Crystal Location Start - End (mm)	Measurement Area Start - End (mm)	Electric Fields (V/cm)
1	4	10	0.6 - 22.7	11.1 - 17.7	17.6
2	7	9	0.6 - 23.4	10.6 - 17.8	18.5
3	7	9	0.6 - 22.8	10.5 - 18.1	20 (x5)
4	8	8	1.1 - 22.0	10.1 - 17.8	21.2 (x2)
5	8	8	0.8 - 22.3	10.5 - 18.5	11.4, 20.1, 28.8
6	8	9	1.1 - 22.4	10.5 - 18.3	12.0 (x2), 21.1, 30.2
7	9	8	1.5 - 22.8	14.5 - 22.3	18.7 (x3), 27.6 (x2)

Table 3.1: Experimental details for the chips in Figure 3.5. The rings correspond to mini-columns with short-range order, and the spots correspond to mini-columns with long-ranged order. The crystal start location indicates the location where the crystal starts relative to center of the shifted-T injection while the crystal finish is the total length of the elution column after placement of the PDMS reservoir hole (overlapping the channel). The measurement start location indicates the left-most position of the bars in Figure 3.5. In some columns, we made multiple elutions at the indicated electric fields.

image, and (iii) 11 finish-line electropherograms spaced at 50 μm intervals. (Note that the electropherograms at the start/end of a given mini-column are shared with the previous/next mini-column). An automated script written in MatLab identifies the location of the two peak maxima and the full width at half maximum (FWHM) for both the 709 bp and 86 bp fragments in each electropherogram. We only use experiments where these two species are resolved sufficiently ($R_s > 0.75$, where R_s is the resolution given as the ratio of the separation between the peaks and the average of their full-widths at half-maximum value) at the start of the measurement window to facilitate the automated data analysis. The electrophoretic velocity within a given mini-column is obtained by linear regression to the time for a peak to pass through a given position in the channel, as illustrated in Figure 3.4. While we could also obtain data about the rate of increase in the FWHM using the same approach, we will show below that the total band broadening within the entire 8 mm region is so small that the measurements within any mini-column are within experimental error.

3.4 Results

3.4.1 Mini-column characterization and experimental parameters

Our data analysis method requires constructing and analyzing thousands of electropherograms, which necessitates automated data processing. Of the 10 columns that we fabricated, there are 7 columns that have elutions that meet our resolution criterion. These columns are

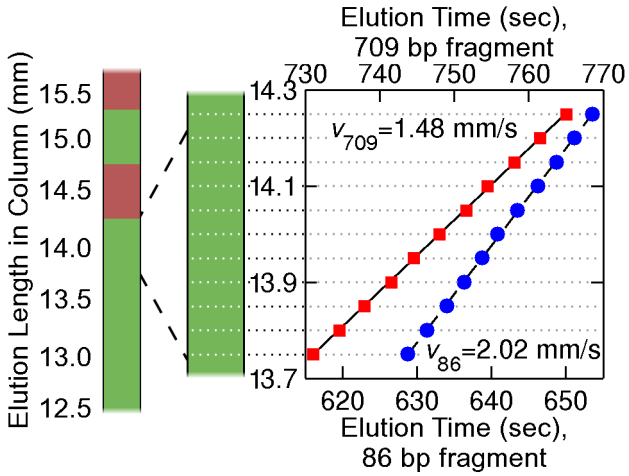

Figure 3.4: Following the principle illustrated in Figure 3.1, the column is conceptually divided into 0.5 mm long mini-columns. Each mini-column has a corresponding white light Bragg diffraction and laser diffraction image, as illustrated in Figure 3.3, with red schematically indicating "ring" diffraction and green representing diffraction "spots". Within a given mini-column, we use the fluorescence intensity $I(x,t)$ data to construct 11 finish-line electropherograms within the mini-column spaced at 50 μm intervals. For each electropherogram, we obtain the maximum peak intensity and the full width at half maximum (FWHM) for both the 86 bp and 709 bp fragments. The figure here plots the average time for the band to pass through a given position. The electrophoretic mobility within a given mini-column is obtained from the slope of these lines divided by the electric field, in this example 21.2 V/cm.

illustrated schematically in Figure 3.5. We adopt a binary classification for the crystalline ordering within a given mini-column based on the diffraction pattern obtained in a ≈160 μm beam spot at the center of that mini-column.

The mini-columns with short-range order tend to occur towards the injection region, which would be expected based on our intentional increase of the crystal growth rate during the assembly process. However, as we can see in chip 6 of Figure 3.5, it is also possible to have interspersed regions of long-range order and short-range order throughout the column. Figure 3.5 also shows each analysis region aligned with respect to the absolute position within the channel. The analysis regions all start at similar (but not exactly equal) locations within the microchannel.

In many of the chips, we ran experiments at multiple electric fields to acquire additional data. Table 3.1 reports the different applied electric fields, ranging from 11.4 V/cm to 30.2 V/cm, used for each of the chips in Figure 3.5. Explicitly, these are the nominal electric fields inside the colloidal crystal. These electric fields constitute the 21 experiments in these chips that had well-resolved separations at the entrance of the measurement window. There

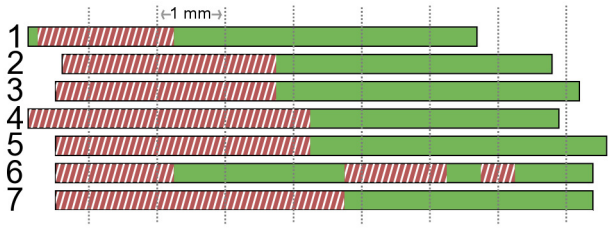

Figure 3.5: Schematic depiction of the regions of long-range order and short-range order in the 7 chips used for the experiments. The color code indicates the type of crystalline order in a given 0.5 mm mini-column, with red hashes and green solids signifying "rings" (short-range order) and "spots" (long-range order), respectively. Examples of each type of ordering are presented in Figure 3.3. The dashed lines indicate the locations of every other ruler marker in Figure 3.2. The leftmost line is the first 1 mm position marker; the exact distance from the injection can be found in Table 3.1. Each elution column is marked to the left with its chip number.

were six experiments in the chips in Figure 3.5 at other electric fields and three separate chips that either did not yield sufficient resolution at the entrance to the measurement window or had poorly-controlled injections. These data produce systematic errors in our automated data analysis program, and it is infeasible to analyze all of the electropherogram data by hand. As a result, we do not use the data obtained from these other experiments.

3.4.2 Electrophoretic mobility

As indicated in Table 3.1, we have obtained data at different electric fields in our experiments. Figure 3.6 confirms that the electrophoretic mobility is independent of the electric field strength for these experiments. These data were obtained by measuring the time corresponding to the peak passing through the start and end of the viewing window, corresponding to an average over all of the mini-columns within a given elution. The different offsets for different elutions indicate shifts in the background electroosmotic flow. Our mobilities are within the range of those commonly seen in agarose gels for similarly-sized DNA [41].

The separation between two species in the colloidal crystal arises from their relative mobilities. Thus, a natural question to ask is whether this mobility ratio depends on whether the DNA are moving through a region with long-range order (spots) or short-range order (rings). The mini-column dataset as a whole ($n = 338$) has a mobility ratio of 1.20±0.11, while the low-order "ring" ($n = 166$) and high-order "spot" ($n = 172$) populations have ratios of 1.14±0.11 and 1.25±0.10 respectively. In Figure 3.7, the box plots show the shape of the population, and the t-test results are shown between the two populations. Each

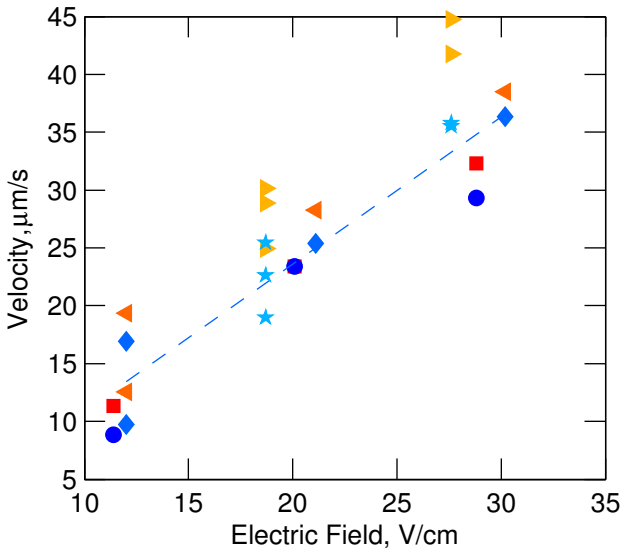

Figure 3.6: Plot of the velocity vs. electric field confirms a linear scaling, characteristic of Ogston sieving, for the three different chips in which multiple fields were tested (chips 5-7). The line shown is a fit of the data from Chip 6, 709 bp DNA ($\diamond, R^2 = 0.93$). The R^2 values for the other fits are: Chip 5, 86 bp ($\square, R^2 = 0.99$); Chip 5, 709 bp ($\circ, R^2 = 0.94$); Chip 6, 86 bp ($\triangleleft, R^2 = 0.94$); Chip 7, 86 bp ($\triangleright, R^2 = 0.94$); Chip 7, 709 bp ($\star, R^2 = 0.91$).

t-test tests the null hypothesis that the two populations, long-range order and short-range order, are indistinguishable from each other. The means of each population are shown with the accumulated measurement error from fitting, with the confidence interval from the t-test shown in between these two means. As we see in Figure 3.7, the populations are indistinguishable from each other in the t-test confidence interval within the stated error. Although there is a difference between the means of the ring and spot populations, the null hypothesis is supported to within the experimental error.

While the mobility ratio in Figure 3.7 is the key factor of interest for separations, it is possible that long-range order (or lack thereof) can lead to a change in the mobilities of each species while leaving the mobility ratio fixed. However, as we see in the box plot and t-test for Figure 3.8a, there is again no statistically significant difference between the populations of mobility data for the long-range order and the short-range order. Although the mobilities for the 86 bp DNA appear to be slightly higher in the ordered region, the difference is within the experimental error and the null hypothesis is still valid. Some of the variability in the mobility data may be attributable to Joule heating raising the temperature of the buffer. However, this would not affect our statistical conclusion as any fluctuations in temperature are included in both "ring" and "spot" data sets by the nature of the mini-column measurements.

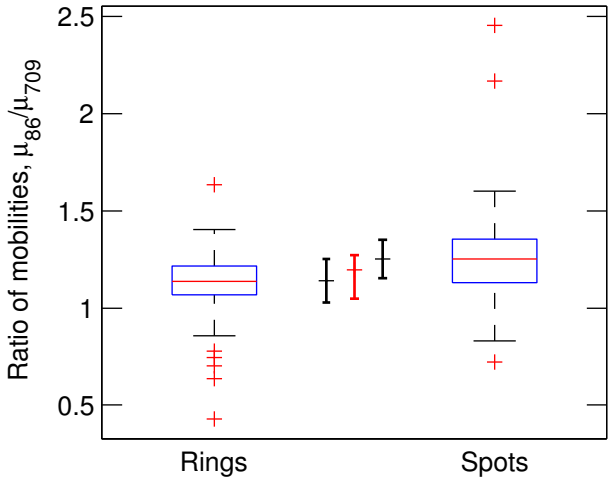

Figure 3.7: Mobility ratio in the regions of short-range order (rings) and long-range order (spots). Each population is shown as a box plot, which depicts the quantiles of the data. The tails represent the extremes of the data, minus the outliers plotted as red +s. The line in the middle of each box is the median value of that data set. The box itself contains the middle 50% of values in the population. Between each of the data sets in black are the population means with the measurement error due to fitting. The red in the middle of the figure is the confidence interval from a two-tailed Student's t-test, variances unknown. This value is plotted as a confidence interval centered between the means of the populations tested, as it tests the assumption that the difference between those means is indistinguishable from zero.

Although we have collected densely packed (50 μm interval) finish-line data from our electrophoresis experiments, one might think the mini-column length of 0.5 mm is not sufficient to determine an accurate electrophoretic mobility. We believe this is not the case, as the representative data in Figure 3.4 exhibit a clearly defined electrophoretic mobility. However, to ensure that our conclusions based on Figure 3.8 are robust to the size of the mini-column, we took all adjacent mini-columns with the same classification in Figure 3.5 and merged them into 1 mm long "two-column mini-columns" before we did the fitting depicted in Figure 3.4. This coarser length scale naturally reduces the size of the populations, but we see in Figure 3.8b that our conclusion is robust; even with 1 mm long mini-columns, the null hypothesis is verified.

The most likely location for a change in the mobility would be in the transition between a region of long-range ordering and short-range ordering, or vice versa, because the DNA must traverse a grain boundary and a change in crystal orientation. Moreover, it is known [39] that DNA tends to travel along grain boundaries in ordered micellar systems, leading to a qualitative change in the mobility compared to transport through the packed bed. The

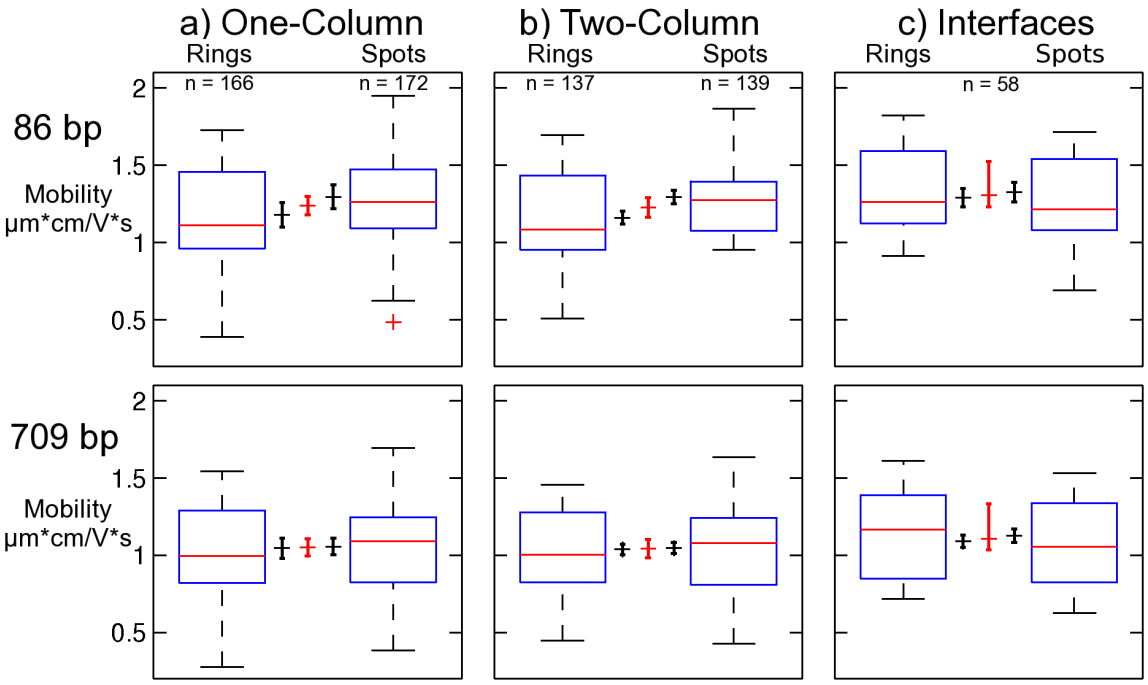

Figure 3.8: Comparisons between long-range order and short-range order populations under different conditions: (a) all mini-columns, (b) merging adjacent mini-columns with the same classification, and (c) at the interface between each type. Each population is shown as a box plot, which depicts the quantiles of the data. Between each of the data sets in black are the population means with the measurement error due to fitting. The red marker in the center is the confidence interval from a two-tailed Student's t-test, variances unknown.

number of such interfaces (see Figure 3.5) is not very large, so the population sizes are small. Nevertheless, the box plots and t-test data in Figure 3.8c show that, once again, the null hypothesis is valid and there is no statistically significant change in mobility moving across the interface.

3.4.3 Band broadening

While we were able to produce the large populations of mobility data in mini-columns possessing long-range order and short-range order required for statistically meaningful conclusions, we were not able to reach the same conclusions about the band broadening because the rate of band broadening is very slow. To make this clear, we computed the increase in the FWHM, $\Delta \equiv \text{FWHM}_{\text{out}}$ - FWHM_{in}, across each mini-column within a given elution and the standard deviation of Δ for that elution. Figure 3.9 shows the mean of Δ for a single elution, divided between "rings" and "spots". We see similar characteristics in all

our elutions — namely that the FWHM changes very little over our 0.5 mm mini-columns, and that there is no discernible difference between broadening in "rings" and broadening in "spots." Additionally, we estimate that the accuracy of any measurement of the FWHM is the scan time, which is 4 seconds. Inasmuch as the variance of the measured values of Δ in a given experiment are normally within the measurement error, we cannot make any meaningful statements about the different band broadening in regions of long-range order and regions of short-range order. Moreover, when looking at the scan data, there are a number of experiments where the peaks appear to sharpen, which we attribute to the experimental error in measuring such small changes in the FWHM, as we can find no systemic reason for these results. Finally, the band broadening data imply that we have avoided any shear- or dye-induced cleavage of the DNA. Different size fragments have different mobilities, so cleavage into a range of fragment sizes would substantially increase the rate of band broadening. Our low band broadening argues against any such breakage.

3.5 Discussion

The goal of our study is to address the importance (or lack thereof) of long-range ordering on DNA electrophoresis in the Ogston sieving regime. The Ogston sieving model was originally developed [14–16] to describe how agarose gel concentration affects the mobility of small, globular-like molecules. The model requires the average pore size of a random network of fibers, then uses this pore distribution to find the fractional volume, $f(c, R_g)$, that a molecule of radius of gyration R_g is able to visit in a gel of concentration c. The key conclusion of the Ogston sieving model is that the electrophoretic mobility in the gel relative to the free solution electrophoretic mobility is proportional to the fractional volume, $\mu/\mu_0 \sim f$, independent of the details of the microstructure of the separation medium. Indeed, one should be able to apply the Ogston sieving model to both disordered and ordered media. We should point out that the assumptions of the Ogston sieving model have been challenged by Slater and coworkers in a detailed series of publications [42–52] using lattice Monte Carlo models of particles moving in tortuous networks. While these works illustrate quantitative disagreement with the Ogston predictions, Slater and coworkers maintain that the Ogston model is still useful to describe qualitative behavior without particular knowledge of the structure of the sieving matrix.

We confirm here that our experiments indeed take place in the Ogston sieving regime. While a colloidal crystal possesses at least short-range ordering, the model only requires specifying the fractional volume available to the DNA. However, it is important that the

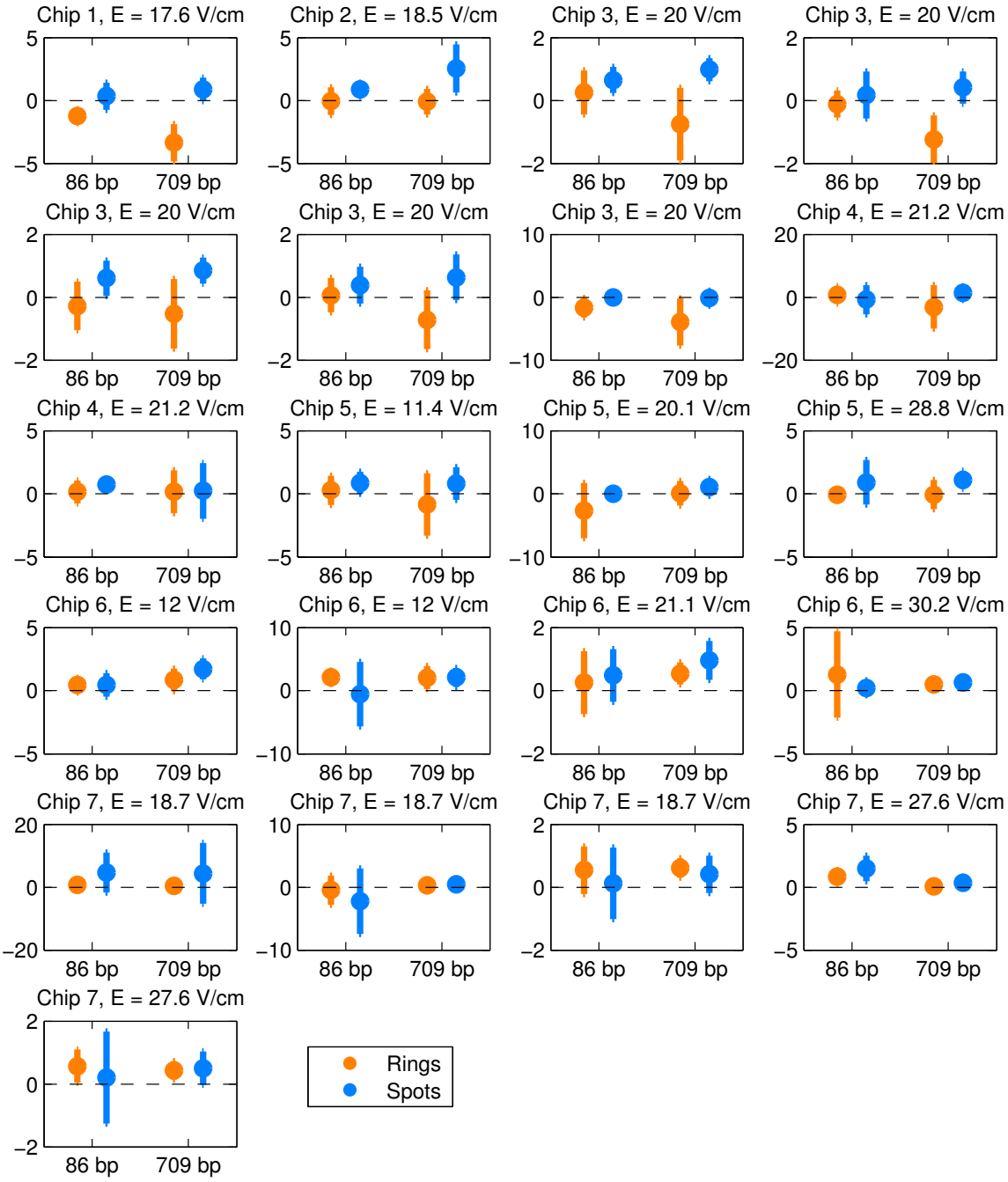

Figure 3.9: The average change in the FWHM across a mini-column in seconds, sorted by DNA size and crystal quality. The error bars correspond to one standard deviation of the mean.

DNA be small compared to the size of the pores. Using a wormlike chain model for the DNA [53] with a persistence length of 53 nm [54] and assuming a 30% increase in contour length from the intercalating fluorescent dye [55–57], we find $R_{g,86} = 10$ nm and $R_{g,709} = 59$ nm. Zeng and Harrison [9] proposed to use a value of 15% of the colloid diameter d to roughly represent the size of the throat connecting interstitial spaces of the crystal, based on fitting a touching sphere. The throats are narrower than the interstitial spaces, which correspond to 41.4% of the colloid diameter for a site of octahedral coordination and 22.5% for tetrahedral coordination and are periodically distributed [7]. However, the 15.5% width of the throats form a useful limiting case for our interests. With a nominal colloid diameter of 900 nm, the throat size corresponds to a radius of 70 nm. The radii of gyration of our DNA are smaller than the narrowest pore space inside the crystal, and much smaller than the centers of the pores. Thus, from a geometric perspective, our experiments are taking place in the Ogston sieving regime.

In addition to satisfying the geometric criterion, it is also essential to confirm that we satisfy the dynamic criterion of the Ogston sieving theory. The assumption that the mobility is proportional to the fractional volume available to the DNA requires that the DNA be able to sample its configurational space during the transit through a given pore. In other words, the Ogston sieving model applies to near-equilibrium separations. Similar geometries can yield non-intuitive behavior [51,58] when the transit time is shortened due to a strong electric field and the separation is far from equilibrium. To assure the molecules have sufficient time to sample these spaces, we can compare their convection time to their self diffusion time, otherwise known as the Péclet number. The fastest molecule we measured has a speed of nearly 50 μm/s, which travels the interplanar spacing distance in $\tau_v = 1.5 \times 10^{-2}$ s. Using diffusion coefficients calculated via the wormlike chain theory of Yamakawa and Fujii [59] ($D_{86} = 34.9$ μm^2/s, $D_{709} = 7.9$ μm^2/s, assuming a viscosity of 1 cP and $T = 298$ K), we arrive at self-diffusion times of $\tau_{s,86} = 3.0 \times 10^{-6}$ s and $\tau_{s,709} = 4.5 \times 10^{-4}$ s. The corresponding Péclet numbers, $\mathrm{Pe}_{86} = 2 \times 10^{-4}$ and $\mathrm{Pe}_{709} = 3 \times 10^{-2}$, are both small compared to unity. As a result, the dynamic assumption of the Ogston sieving model is satisfied.

Finally, we also need to confirm that the regions with short-range order and those with long-range order have the same pore sizes. The laser diffraction measurements provide a very convenient way to address this question, since the laser diffraction patterns are analogous to a Fourier transform of the three-dimensional correlations of each colloid within the spot of the laser beam. A perfectly-ordered colloidal crystal diffracts into clean, bright spots. We see this in Figure 3a, implying that within the entire area of the beam, each

colloid's nearest-neighbor orientations are identical. If, instead, we have within our interrogating beam many small grains with unique orientations, each grain will have their diffraction spots at unique rotation relative to the other grains. Overlaying many of these patterns will yield a diffraction ring as seen in Figure 3c, and implies that within our beam there are many changes in crystalline orientation. However, the first-order diffraction information (either spots or rings) is located at the same distance, which confirms a consistent nearest-neighbor distance. Our columns are thus close-packed, independent of the long-range ordering, implying a uniform pore size throughout the medium.

Given that our system satisfies all of the conditions for Ogston sieving: geometric freedom (R_g smaller than free space) and dynamic freedom (self-diffusion time much smaller than inter-pore transit time), it is reasonable to compare the model predictions to our experimental data. The Wirth group recently developed a model for protein electrophoresis (adapted from the original Ogston sieving fractional free volume assumptions) in colloidal crystals [26], which, given a porosity ϵ and colloid diameter d, provides the electrophoretic mobility

$$\frac{\mu}{\mu_0} = \epsilon \left[\frac{(d - 2R_g)^2}{d^2} \right] \tag{3.1}$$

If we assume that both our 86 and 709 bp species have the same free solution mobility μ_0 [60], we can rewrite Equation 3.1 as the ratio

$$\frac{\mu_{86}}{\mu_{709}} = \left(\frac{d - 2R_{g,86}}{d - 2R_{g,709}} \right)^2 \tag{3.2}$$

Using the values of $R_{g,86} = 10$ nm and $R_{g,709} = 59$ nm for a worm-like chain [53] with our $d = 900$ nm colloids leads to a mobility ratio of 1.27, which agrees with our measured value of 1.20 ± 0.11. This is further evidence for our separation taking place in the Ogston sieving regime. Additionally, as shown in Figure 3.6, we see a linear increase of the velocity with an increasing electric field. This result is also consistent with the Ogston sieving model, which predicts no dependence of the mobility on the electric field (all fits have $R^2 > 0.91$).

We can thus view the statistical study in Figure 3.8 as confirmation of the basis for the Ogston sieving theory for the electrophoretic mobility; if we make a pore network with a relatively uniform pore size distribution, then the electrophoretic mobility is independent of the connectivity between these pores. Indeed, the Ogston sieving theory makes no consideration of overarching geometry or symmetry, and therefore does not account for the presence or absence of long-range order. Provided that the DNA are unable to experience any length scale larger than the individual pores, they should only be subject to the distribution of

pore sizes as a whole, and not the arrangement of these pores with respect to each other. We posit that the experiments here provide a stringent experimental test of the mean-field basis for the ubiquitous Ogston sieving theory, on par with the theoretical studies by Slater and coworkers [42–52].

While we might have expected the electrophoretic mobility to be independent of the long-range ordering, the Ogston sieving theory does not provide any insights into the band broadening. Moreover, since the band broadening arises from deviations from the mean electrophoretic velocity, it is reasonable to suspect that the band broadening might be impacted by transport across (and possibly along) the grain boundaries of the crystal. However, our results in Figure 3.9 indicate that the band broadening is negligible throughout the entire device.

Our band broadening results for DNA electrophoresis are also consistent with data obtained for protein separations [10,20,26] and DNA separations [9]. To make this comparison, we use our scan data and convert our FWHM to standard deviations as $\sigma = (2e^{-1/2})\text{FWHM}$, which we use to calculate a dispersion (effective diffusion) coefficient from $\sigma^2 = 2\bar{D}t$. The corresponding plate height of $H = 2\bar{D}/\bar{U}$ is obtained using an average velocity $\bar{U} = \mu E$. By calculating the difference between the first and last appearance of each full peak in our measurement window, we obtain an average plate height of 14.1 μm and 3.6 μm for the 86 and 709 bp peaks respectively. These results compare favorably with prior work [9, 10] in DNA electrophoresis, which reported micron scale plate heights. The plate heights are larger than the sub-micron values obtained by Wirth and coworkers [20] for chromatographic protein separations using colloidal crystals in capillaries. Their crystals were created by wicking and drying of a colloidal suspension, yielding a similar polycrystallinity to our crystals formed by CSA. While the protein separations are chromatographic, relying on the different adsorption affinity of the proteins to the solid support, the geometry and transport rates for their proteins and short DNA are similar. However, it is not clear whether the smaller plate heights in the protein separations are due to the different mechanism of the separation or other differences in the experimental protocol.

Addressing the fundamental question of the role of order on DNA electrophoresis in the Ogston sieving regime impacts applications of colloidal crystals for DNA separations. Explicitly, our results indicate that quality separations within the Ogston sieving regime do not require crystals with long-range order. Creating extremely long, ordered crystals inside a microchannel is extremely challenging. The boundary conditions imposed by the walls can frustrate the formation of crystalline order; even if the channel is very wide compared to the colloid diameter, nucleation events at the channel walls can propagate deep into

the channel. While straight side walls (or even epitaxial patterns [61]) can relieve the packing frustration, we need to ensure that the channel dimensions are an integer multiple of the colloidal interplanar spacing. Even with a perfect channel, growing a high quality crystal also requires exquisite control over the growth conditions such that a single grain can dominate during growth. These controls are relatively well-developed for crystal growth on flat substrates, but careful growth in microfluidic devices is refined only to the point of slowing the growth rate, thereby taking hours to days to complete. One exception to the slow growth requirement are colloidal crystals assembled on templated substrates [62]. Unfortunately, these packings are too small to be useful for separation. Also, the failure rate (crystals that grow poorly) will be much higher from the stricter requirements, adding significantly to the overall experimental overhead. Our results indicate that quality DNA electrophoresis separations within the Ogston regime require nothing more fabricationally-intense than a close-packed crystal. As a result, separation media can be created in minutes and will almost certainly be of adequate quality.

3.6 Concluding Remarks

In the present contribution, we have conclusively demonstrated that long-range ordering does not play a role in separations of short DNA in colloidal crystals which are much larger than the DNA. The literature thus far [9,10,20,21,26] describes these separations as having Ogston sieving-like behavior, where the mobility depends primarily on free volume available to the molecule at relatively low fields. The Ogston sieving theory is a mean-field approximation of the free volume, and therefore has no dependance on the order of the matrix. It also makes no predictions of band broadening, which could be affected by this ordering. We found that, under a host of metrics, the long-range order has no measurable effect on the broadening, nor the relative or absolute mobilities of the DNA. Our results relied heavily on an experimental protocol that rapidly generates large numbers of finish-line electrophoregrams, coupled with on-device characterization of the sieving medium. From a single elution experiment, we were able to generate more than 150 finish line electropherograms, all taken at known positions and under the same experimental conditions. The conclusions about order developed from our experiments support the use of quickly and inexpensively fabricated devices, requiring only a close-packed crystal and having no requirements on grain size.

Our band broadening results are consistent with prior work in DNA separations [9,10], with the colloidal crystal exhibiting minimal band broadening. In our case, the band width appears to come primarily from the width of the initial injection band. Combining our

results with prior work using bidisperse colloids [19], it seems that the key to the low band broadening during DNA electrophoresis in colloidal crystals is their close-packed nature, not their crystallinity. So long as the colloids are monodisperse and close-packed, the pore sizes are well defined and uniform throughout the material. If the colloids are not monodisperse [19], then there is band broadening due to the different pore sizes. If the colloids are not close-packed (i.e., if there is a crack), then the DNA tends to migrate along the crack rather than through the interior of the crystal [9, 19, 21]. This destroys the separation as it introduces significant radial heterogeneity in the mobility, creating catastrophic band broadening as well as providing a sieve-free path.

The results obtained here apply to DNA molecules that have radii of gyration that are small compared to the colloid size. In principle, we can scale-up a colloidal crystal separation matrix to larger size colloids, thereby separating kilobase-scale DNA via Ogston sieving. In practice, one is more likely to use the same colloid size to separate DNA over a range of molecular weights [9]. When the radius of gyration of the DNA exceeds the pore size, the separation mechanism switches from Ogston sieving to entropic trapping and eventually to biased reptation [4]. While we would anticipate that long-range order would have a minimal role in the entropic trapping regime, since the DNA only see the neighboring pores, we expect to see a qualitatively different effect of long-range order during biased reptation. In these situations, an individual molecule will span multiple pores and itself sense changes in pore orientation relative to the electric field direction. The experimental techniques described here are ideally suited to address this issue.

Chapter 4

Separation Behavior of Long DNA

4.1 Introduction

Colloidal crystals, originally investigated for their unique optical properties [5, 17, 24, 25, 32, 33, 35, 61, 62], have seen recent use in a variety of biomolecule separations and studies [8–10, 18–23, 26, 36, 63]. Commonly, the colloidal crystals are grown from monodisperse colloids within a microfluidic device through convective self-assembly, a process that creates repeatable, close-packed structures [6, 9, 25, 63]. These microfluidic devices are filled with an electrophoresis buffer, which infiltrates the crystal. The biomolecules to be separated are driven through the device either electrophoretically or fluidically, being separated by size within the colloidal crystal, which acts as a sieving matrix. These separations have shown remarkably low band broadening [10,20,63], encouraging their further study. Indeed, colloidal crystals for protein chromatography are now commercially available from bioVidria, a startup formed in part by Mary Wirth.

Early work on DNA electrophoresis in colloidal crystals compared the sieving abilities of colloidal crystals to those of agarose gels [8, 9, 21]. The comparison was drawn between comparable pore sizes in colloidal crystals and agarose gels. In crystals, the pore most commonly referred to is the narrowest constriction in the lattice – the neck between interstitial sites. This has an exact size of $0.155d$, where d is the diameter of the colloids. Using this length scale to characterize the separation medium is appropriate for DNA much smaller than the neck, but larger DNA (such as the 48.5 kbp λ-DNA we will study here) will span multiple interstitial spaces [8, 22], which can fit a sphere with diameter $0.414d$. Regardless of the length scale used to quantify the pore size, previous researchers used colloidal crystals to perform separations that would be nearly impossible in their comparable agarose gels [3, 9]. We believe that this seeming impossibility is a sign that agarose gel concepts

are an inadequate explanation for the behavior of DNA in colloidal crystal sieves. The quick and efficient separation of large DNA molecules is very desirable [31], and if colloidal crystals are going to be part of that future then they demand a closer look.

Zeng and Harrison [9] presented the most systematic study of DNA separations in colloidal crystals to date. They proposed that separations in a crystal formed from 900 nm colloids performed similar to a 2% agarose gel. The behavior of small DNA (<1 kbp) in a 2% agarose gel is described by the Ogston sieving model [14–16], which predicts a mobility independent of the applied electric field. For DNA much larger than 1 kbp, the mobility is described by the biased reptation with fluctuations (BRF) model [64–66]. This model predicts a mobility independent of the field at very low values of the electric field, known as biased reptation without orientation, that transitions to a linear field dependence as E increases and the DNA transitions to biased reptation with orientation [67]. In the case of a 2% agarose gel, the transition between field-independent and linear dependence on the electric field occurs at field values below 0.13 V/cm for λ-DNA (the lowest field tested by Heller *et al.* [3]). The linear scaling was also seen in 1 μm diameter silica colloidal crystals by Meistermann and Tinland [8]. Importantly, the BRF model predicts that all DNA will exhibit the same electrophoretic mobility during biased reptation with orientation. Thus, if the DNA mobility is linear in the electric field, no separation should occur.

In the previous Chapter we tested the assumption that the same mean-field theories used for DNA electrophoresis in agarose gels could be used to describe the motion of short DNA fragments in colloidal crystals. In gels, the mobility of these small DNA (<1 kbp) is described by the Ogston sieving theory, which accounts for the average free space available to the molecule relative to that molecule's size [14–16]. We found that this agarose gel model performed well to describe our close-packed system, a conclusion echoed by the simulation work of the Wirth group for protein separations [26]. As the Ogston sieving theory applies to only those DNA much smaller than the available free space, it cannot be used to describe λ-DNA in micron-sized colloids.

In agarose gels, these long DNA are described by more rigorous treatments of the DNA as a polymer chain [4,64–66], and it is these theories we propose to evaluate in this chapter. The seminal work confirming BRF in agarose gels was performed by Heller *et al.* [3]. They tested the relationships between DNA size, agarose gel concentration, applied electric field, and the observed mobility of the DNA by running hundreds of very careful gel electrophoresis experiments. Their results agreed quantitatively with the predictions and simulations of Duke *et al.* [66] for biased reptation with fluctuations.

There do exist limited data for the mobility of long DNA in a colloidal crystal. Meistermann and Tinland [8] measured the mobility of single molecules of large DNA in 1 μm diameter colloids, finding confirmation of the BRF theory in colloids. They noted that even in fields lower than 10 V/cm λ-DNA did not exhibit a field-independent mobility, instead always remaining linearly dependent on the electric field. By contrast, they found that 5721 bp DNA was field-independent up to $\sim$15 V/cm, at which point its mobility became the same as the larger DNA. Zeng and Harrison [9] showed an impressive separation of very large DNA molecules, λ-DNA (48.5 kbp) from T4 DNA (166 kbp) and λ-DNA from calf thymus DNA [9]. These separations would be impossible if performed under a direct current in the agarose gels chosen to represent the 1600 and 900 nm diameter colloidal crystals used, respectively, for the separation of λ-DNA from T4 DNA and from calf thymus DNA, as well as from the experiments of Meistermann and Tinland [8].

As we noted previously, the biased reptation theories predict a limit of separation, where the mobility is no longer dependent on the molecular weight. Heller *et al.* [3] found the behavior of this separation limit, N^*, to be similar the BRF predictions of linear scaling with the inverse of the applied field. In the 2% agarose gel that Zeng and Harrison [9] claimed would be a reasonable model for 900 nm colloidal crystal sieves, a 1 V/cm applied field would be unable to separate DNA molecules much longer than 5 kbp [3]. However, Zeng and Harrison [9] showed the separation of DNA between 100 and 2000 bp in length in 900 nm colloids using electric fields up to 27.9 V/cm, which a $N^* \sim E^{-1}$ extrapolation from the work of Heller *et al.* [3] would lead to a value of $N^* = 500$ bp – a molecule too small to coil between multiple pores and therefore outside of the biased reptation description. This cutoff is much lower than the separation between 2 and 1.2 kbp fragments separated by Zeng and Harrison [9], which occupy $\sim$1 and 2 pores respectively (from a random walk blob theory argument and $0.155d$ as the pore radius [68]).

Can one use DNA gel electrophoresis theories to explain the impressive separations of Zeng and Harrison [9]? While a few theories have been proposed describing large DNA mobility in colloidal crystals as either biased reptation or entropic trapping [9, 18, 19, 21], none of these descriptions deviate significantly from their agarose gel-derived roots.

In this chapter we examine the adequacy of DNA gel electrophoresis scaling models to predict the mobility versus the electric field for large DNA molecules. We emphasize that an oversimplified explanation of the crystal geometry will never truly suffice for explaining the electrophoretic sieving of DNA by colloidal crystals. Therefore, in an attempt to better understand the separation behavior of long DNA molecules, we follow the spirit of the seminal work of Heller *et al.* [3] in this unique medium to examine the mobility of λ-DNA

in colloidal crystals. We measure here the mobility of λ-DNA as a function of the applied electric field. We observe the entire elution of the DNA throughout our colloidal crystal and vary the electric field during that elution. To control for day-to-day experimental variations, we include a ladder of small, <1 kbp DNA to act as tracers. Our methodology offers the distinct advantages of eliminating entrance effects from our subsequent mobility measurements and facilitates rapid testing of the mobility (μ) versus applied electric field (E) space. We trade some capability in measuring very slow moving DNA as a result of making more frequent measurements, but gain a marked increase in experimental throughput relative to the methodology of Heller *et al.* [3]. This chapter compares the results gained from these methods and evaluates them against the established agarose gel theories for the transport of large DNA.

4.2 Materials and Methods

We chose to use two standard DNA samples from New England Biolabs, λ-DNA and their own PCR Marker to mimic in colloidal crystals the work of Heller *et al.* [3] for agarose gels. The λ-DNA is 48.5 kbp and is one of the most ubiquitous DNA molecules in long DNA separation literature. The PCR marker is comprised of five fragments: 50, 150, 300, 500 and 700 bp long. The stock concentrations are 500 and 300 μg/ml, respectively, allowing for relatively high concentrations in any final mixtures. We use the small DNA to confirm our crystal is separation-grade – no cracks or partial blockages.

When splitting the DNA fluorescence signal between six bands we were cautious to start with as high an injection concentration of DNA as possible. Our final DNA concentrations were 150-200 μg/ml. These high concentrations of DNA required us to lower the ratio of YOYO-1 dye molecules (Invitrogen) to basepairs from the 1:5 of our previous work to roughly 1:15. Our early experiments using the higher dye concentrations were plagued by sticking and clumping of the DNA, which were alleviated after lowering the dye concentration.

We used the same microfluidic channels described in our previous chapter 3. We use a shifted-T design with four reservoirs – a source, two wastes, and the separation output. The separation arm is 25 mm long, while the other three arms are 5 mm long. The channels are ≈100 μm wide by ≈20 μm deep. The channels are wet-etched into soda lime glass and sealed into microfluidic devices with a polydimethylsiloxane (PDMS) lid. Prior to growing the crystal, the PDMS lid was soaked overnight at room temperature in 2.5x TBE. The soaking, which we did not use previously [63], eliminated some uneven fluid flow within

the crystal during separation, which led to stacking of the DNA approximately halfway down the elution arm. We suspect that the crystal was drying out and therefore the DNA was able to move until impeded by the opposing permeation flow, which was evaporating through the water-permeable PDMS at the point furthest from any reservoirs – the center of the separation arm [69]. This change in procedure required each device to be used shortly after crystal growth, allowing 30-90 minutes of equilibration between cessation of crystal growth and addition of running buffer. The running buffer was 2.5x TBE (Tris base, Boric acid and EDTA) with 0.06% polyvinyl pyrrolidone and ascorbic acid.

Our separation data are collected using a modified approach to scanning electrophoresis [29]. We use a custom LabView routine to control a PriorScan automated microscope stage, attached to an inverted Leica DMI-3000B microscope. We use a halogen light source through a filter cube designed to emit blue light (centered around 491 nm), which excites the fluorescent dye YOYO-1 and collects the emitted light (centered around 509 nm). This light is collected by a Hamamatsu photomultiplier tube (PMT), which outputs a signal voltage proportional to the light intensity. The LabView program records both the stage position and PMT voltage versus machine time as the illumination pans back and forth along the separation arm of our microfluidic device. The electric fields are controlled using LabSmith Sequencer software and a LabSmith HVS448-1500 high voltage power supply to apply potentials to each reservoir. We use a custom Python script to generate the voltages required for each reservoir by setting a desired electric field in each device arm and specifiying which arm will be the ground. We use as inputs the lengths of each arm and the length of crystal in the separation arm, to account for the different resistance in that arm [63]. The Python script calculates the required voltages for each step of the separation and formats the output to be readable by the Sequencer program. During operation the Sequencer software collects the voltage and current data from each reservoir, which we use in our analysis to calculate the actual applied electric fields in the device. The voltages to set are calculated by assuming the voltage in the assigned ground reservoir, which is typically 450 volts above the power supply ground, and confirmed by measuring the actual potential of the ground in that reservoir during the experiment. This reservoir was floated to prevent overconstraining the electric circuit formed within the microfluidic device.

The programmable power supply allows another step towards increasing experimental efficiency: varying the electric field within a single elution. We use a homemade Python script to generate configurations for the Sequencer software to vary the applied electric field in the separation arm at a set interval, 45 or 50 sec (which is long enough for 4-6 complete scans at a single electric field). This allows us to sweep a range of six to eight electric fields

during each elution with enough time to repeat the cycle at least twice. The fields are chosen to cover a wide range of electric fields and then input in a random order. We scan over the entire separation arm to collect mobility information throughout this cycling. We thus obtain measurements of fluorescence intensity along the entire channel as a function of time, with a quasi-static applied electric field. We use this modified method to generate with each elution a set of μ versus E data – a dramatic increase in throughput from the original experiments of Heller *et al.* [3], where some experiments lasted up to 500 hrs for very low electric fields.

We use an electrokinetic injection common to shifted-T devices [28]. We load the injection area by applying an electric field of 70 V/cm towards the waste reservoir for 30-60 minutes to stabilize the concentration of DNA in the channel. The long load time is used to prevent an injection bias against the λ-DNA, which takes longer to diffuse from the reservoir (where electric field is weak) into the loading channel (where the electric field is strong). The injection field drives the DNA in the injection area towards the separation arm and was consistently 60 V/cm, which was switched to 10 or 15 V/cm shortly after the DNA band entered the crystal. A pull-back voltage of 70 V/cm was applied in the waste and source arms to pull excess DNA back towards the waste and source reservoirs. Once the largest four species (λ-DNA through 300 bp) were sufficiently resolved to identify the peak locations while scanning, we switched the power supply to the automated program that periodically moves between different electric fields. The separation proceeded under the electric field program until all the DNA had passed outside of the measurement window, at which point the original injection fields were reapplied for $\sim$5 minutes to drive the injected DNA completely into the outlet reservoir. Following a visual inspection of the crystal for damage or drying and considering the quality of the previous injection, either a second elution was performed or the device was disassembled for reuse by removing the PDMS lid and washing out the colloids. Each experiment yields the raw data of LabView outputs of position versus time and intensity versus time along with the Sequencer output of current and voltage versus time for each electrode.

The raw data were first processed to combine the LabView's two outputs of position and intensity versus time to an intensity versus position file for each unique scan pass. These files will henceforth be referred to as "scans". Each scan was then run through a second processing step to identify and locate the resolved peaks. As shown in Figure 4.1, these locations were subsequently used as initial guesses for a final Gaussian fit of the available peaks. We used the Gaussian peak fitting to provide more accurate center-of-mass calculations for the PCR marker signals, which are not baseline resolved. The fitted

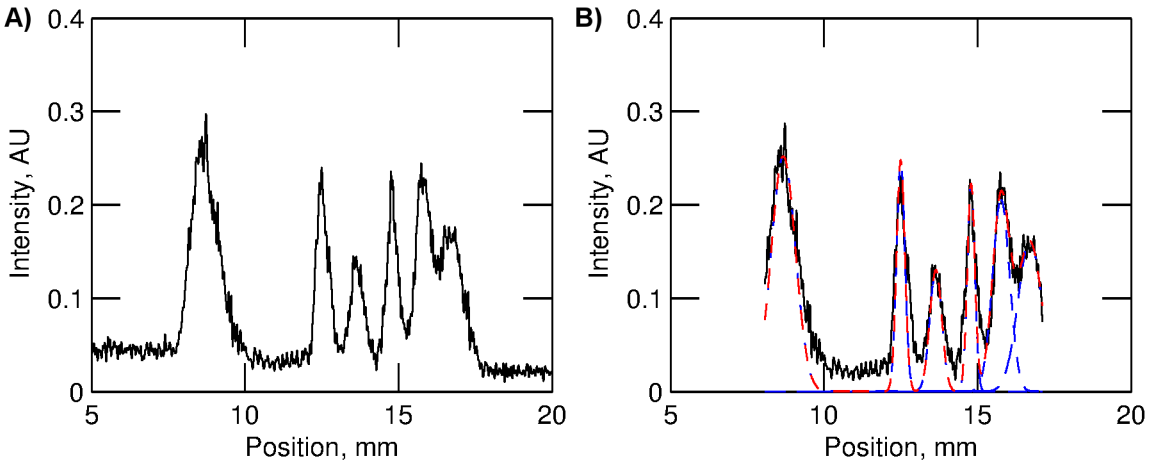

Figure 4.1: An example of the raw data collected by our system. The peaks are, from left-to-right: λ-DNA, 750, 500, 300, 150 and 50 bp. Our first pass system identifies peaks by finding local maxima. These positions are used as initial guesses for the later Gaussian fits, shown on the right.

parameters were output along with the mean scan time of each scan.

For each scan in an elution, we developed a paired list of times and positions for each measured peak. At each value of the scan time, we also calculated the electric field in the separation arm from the potential values returned from the Sequencer porgram, as seen in Figure 4.2A. These values were typically within 10% of the desired value sent to the power supply. Then, for each range of times with a constant electric field, we linearly fit the time versus position data for each peak to obtain the velocity of that peak for a given applied electric field. By dividing each velocity with the electric field used in that cycle, we obtained a list of mobilities versus applied electric field, shown in Figure 4.2C.

For each elution, we were able to test six to eight unique electric fields one to three times each for at least four of the six DNA lengths (depending on whether or not the smallest DNA molecules had resolved at that point) used in the separation. We collected data from four separate devices, with one device yielding three elutions and a second device yielding two for a total of seven elutions. We tested electric fields ranging from 2 to 80 V/cm.

4.3 Results

The results of these experiments are presented in Figure 4.3 as mobility versus electric field. The data have been binned according to the desired electric field values sent to the Sequencer program. The values plotted represent the means of each bin – the full data are

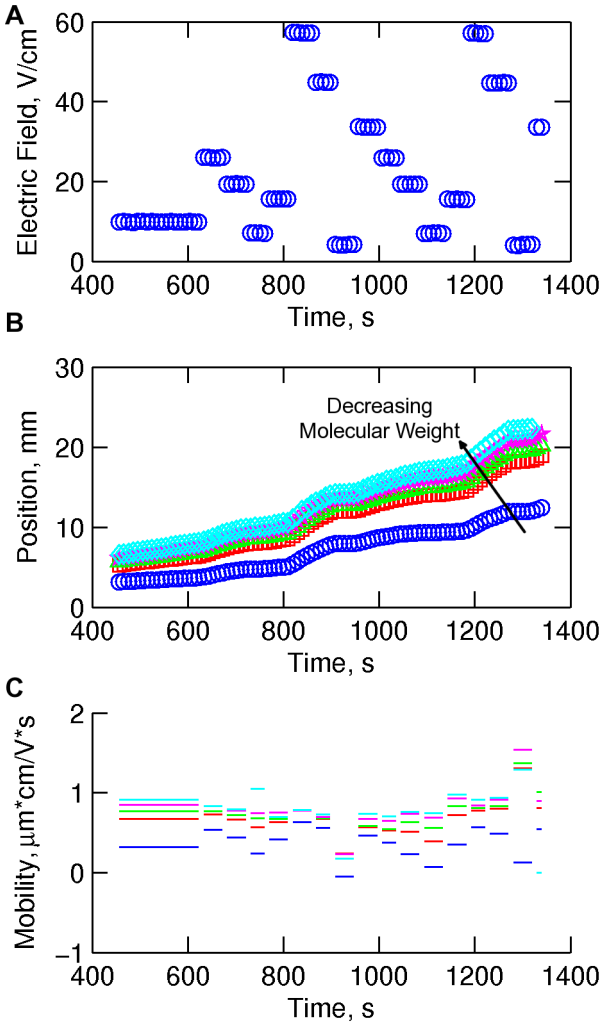

Figure 4.2: The electric field (a) is calculated at the time of each scan. The time regions of constant E are used to define the range of position data (b) to be used to compute the DNA velocity, which when divided by the applied electric field produce the mobility (c). In panel (c), the mobility increases with decreasing molecular weight. ○ λ-DNA, □ 750 bp, ◇ 500 bp, ○ 300 bp, □ 150 bp

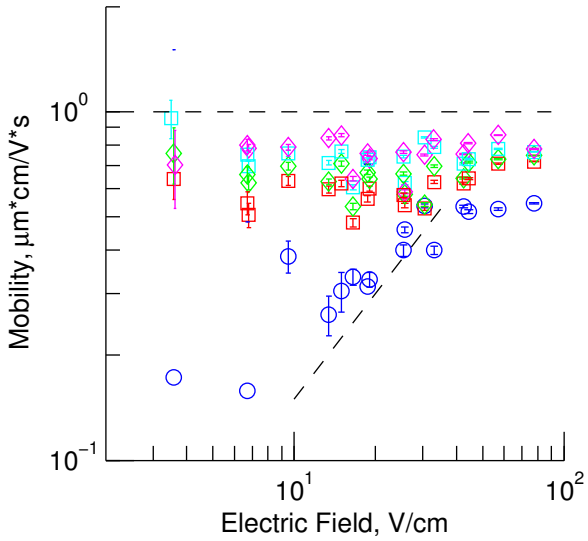

Figure 4.3: Mobility versus the electric field for five sizes of DNA. The dashed lines have slopes, $m = 0$ and $m = 1$. ○ λ-DNA, □ 750 bp, ◇ 500 bp, ○ 300 bp, ◇ 150 bp

given in Appendix B. The two lines in the plot have a zero and linear slope.

As can be seen in Figure 4.3, the small PCR Marker DNA have field-independent mobilities for the entire range of electric fields. This is consistent with the predictions of the Ogston sieving model for small DNA, where the mobility depends only on the free volume available to the DNA molecule [14–16]. This is also in keeping with the data presented by Zeng and Harrison [9] for DNA between 100 and 2000 bp in size between 10.9 and 27.9 V/cm. We also see agreement with the mobility values and scaling measured in our previous chapter 3.

The molecule of interest is the λ-DNA, which exhibits three clear mobility regimes: field-independent from 0 to 10 V/cm, linear with the field between 10 and 40 V/cm, and then saturated about 40 V/cm. The two lower regimes align with those found by Meistermann and Tinland [8], confirming the crossover between regimes is nearly two orders of magnitude higher than that predicted by the BRF theory in comparable gels. We note that Meistermann and Tinland [8] did not observe the lower electric field plateau for λ-DNA, only for smaller (but still coiled) DNA.

The saturation of the mobility above 40 V/cm is similar to the result of Zhang and Wirth [22] phenomenologically, if not quantitatively. They found a mobility saturation for single molecules of λ-DNA above 200 V/cm in 300 nm diameter silica colloids. The plateau observed by Zhang and Wirth [22] is attributed to a decrease in hooking events, where the λ-DNA is wrapped around the neck formed between two touching colloids.

4.4 Discussion

Our data taken below 40 V/cm align well with those of Meistermann and Tinland [8] and Zeng and Harrison [9], which both show a clear E-independent (or weakly dependent) region for $E < 10$ V/cm in colloidal crystals of similar size to our experiments. The onset of the linear orientation regime is two orders of magnitude higher than that for the 2% agarose gels used to compare with 900 nm diameter colloidal crystals. The BRF theory holds that the crossover is proportional to the inverse of the electric field, $N^* \sim E^{-1}$. This crossover also depends on the inverse of the ratio of size available to DNA chain segments, $N^* \sim (a/b)^{-1}$, where a is the pore size and b the Kuhn length. In their discussion of the BRF model, Duke *et al.* [66] provide a value of $(a/b) = 3$ for a 1% agarose gel. It is worthwhile to see how this argument extends to colloidal crystals. The value of b is the same regardless of the sieving matrix (∼100 nm). The pore size, which could be modeled as being anywhere from 140 to 370 nm for 900 nm diameter silica colloids, does not vary by two orders of magnitude. Thus the cause for this shift must point to the insufficiency of the BRF model to fully describe the motion of large DNA in these two lower field regimes.

The third mobility regime of λ-DNA is the high-field saturation regime. This was first observed in colloidal crystals by Zhang and Wirth [22], although at electric fields above 200 V/cm in 300 nm silica colloidal crystals. They attributed the loss of field dependence to a decrease in hooking events as observed by video microscopy of single molecules. Our crossover occurs nearer to 40 V/cm. If we consider hooking alone as a method of retarding the λ-DNA's mobility, then there the area density of necks is $(900/300)^{-2} = 0.111...$, or ∼ 1/10th. This would predict our crossover to be close to 20 V/cm, which is similar to our observed value, given the assumptions made.

We note that, in the discussion of Duke *et al.* [66] on the limits of applicability for the BRF theory, they mention that at high values of the electric field the reptation tube undergoes large oscillations in tube length, while maintaining the same average length. They observed in their simulations the beginnings of a field-saturation effect, which was also seen in the experiments of Heller *et al.* [3] This offers an alternate picture of the root cause of the saturation of the mobility for the λ-DNA in colloidal crystals. The transit of λ-DNA from pore to pore is undoubtedly arrested by collisions with the colloids and hooking around necks, which would contribute to rapid contraction and expansion of the DNA molecule. λ-DNA has a radius of gyration of roughly 0.74 μm and therefore must be stretched within even the largest of pores (a radius of 0.19 μm). Indeed, it should be noted that this pore size is not itself truly indicative of the available space, as it is calculated for a hard sphere fitting within the crystal. The true volume available to the DNA is the

unoccupied 26% of free space with only positive curvature for walls. Also, the insulating silica colloids do not conduct the electric field, giving rise to curved electric field lines [70]. This further complicates our intuitive understanding of both the motion of the DNA as well as along which avenue to begin deviating from established agarose gel theories.

Finally we note that even at our highest applied electric field, 80 V/cm, the saturated mobility of the λ-DNA does not yet approach the mobility of the smaller PCR marker DNA. This mobility difference along with the delayed onset of orientation form a strong argument for succesful separations at electric field values much higher than traditionally used in DNA electrophoresis.

4.5 Concluding Remarks

We have shown above that the models developed for DNA in agarose do not adequately describe the behavior of long DNA in colloidal crystals. Short DNA molecules were used to initiate simple mapping across media, but this map breaks down when considering much larger DNA. Our results indicate that there may not exist a model that describes DNA electrophoretic mobility in colloidal crystals with enough precision to explain our results, or indeed those present in the literature. Prior to their wider adoption as sieves, it will be necessary to more deeply investigate colloidal crystals and their separation behavior. The works of Birdsall *et al.* [26] and Zhang and Wirth [22] are a step in the right direction. The crystalline structures themselves can be readily adapted to a computational experiment. The method employed by Laachi and Dorfman [71] could be adapted to account for the entropic aspect of pore occupation for very large DNA molecules. This could in turn enable the direct measurement of conformations and transport properties that are difficult to do for single molecules in a colloidal crystal separation system.

Even without a deep fundamental understanding of DNA migration in colloidal crystals, it is already apparent that colloidal crystals can function well as DNA sieves over a wide range of electric fields and colloid sizes. There remains unexplored the relationship between colloid size and maximum separable DNA, as well as a more general understanding of DNA transport in these types of devices. We have shown here a technique that can be readily applied to this system as well as others for rapid mapping of separation parameters, and its usefulness has been demonstrated to bring insight and understanding to this new separation medium.

Chapter 5

Reflections and Conclusions

5.1 Development of Data Processing Method

The results presented in my papers and this thesis have the common theme of measurements made of heterogeneous systems. For the first paper, we measured a heterogeneous crystalline packing and its localized effects on separation performance. In the second paper, we looked at a homogeneous separation matrix with a heterogeneous electric field applied. To find the answers to the questions raised by each paper I developed and refined a system built off the principle of Scanning Mode Electrophoresis.

Scanning Mode Electrophoresis was first shown by Lo and Ugaz [29] as a method to take snapshots of gel separations on a microfluidic platform. They took multiple images of a gel separation while moving the microscope stage and later building a coherent image of the separation at that moment in time. It was a novel solution to mimicking the gel electrophoresis standard of snapshot images.

Standard gel separation procedure is to run an unstained DNA sample through the gel at a set electric field for a set amount of time. At the end of the set time, the fields are turned off and the gel is removed from the separation apparatus. The gel, and thus the DNA, are stained with a UV-sensitive dye. After soaking, the stained gel is taken to a UV illuminator and the locations of the DNA bands are recorded. By knowing the separation duration and the distance travelled, one calculates the velocity of each band, which is converted to a mobility by dividing the velocity by the applied electric field. Thus, the researcher gains mobility information by taking a snapshot of the gel after a set amount of time.

Microfluidic separations, by contrast, generally use a "finish-line" approach to collecting mobility information. This is a holdover from the capillary electrophoresis experiments that were intially being miniaturized. In microfluidic systems, the sample mixture is injected into

the separation arm and elutes down the channel towards a fixed sample detector a known distance away from the injection site. As the mixture separates into individual bands, these bands will pass the fixed detector at unique times. These varied times to elute are then combined with the fixed elution length to calculate individual velocities and mobilities for each unique DNA band. In the finish-line methodology, the elution length is fixed and time varies.

Our group's major innovation stems from our desire to automate the Ugaz snapshot method. It was trivial to to automate cyclic scanning of the channel when creating the LabView controller software for snapshots. The initial experiments [72] that used the new software were indicative of the early advantages of this technique. We observed a separation in progress within a unique device geometry, and were able to watch the separation evolve as time progressed in 20 sec snapshots and the analytes progressed down the channel. In stark contrast to finish-line measurements, we could see that our mixture had fully separated long before the end of the device, and was used to build arguments for the separation efficiency of the device as well as confirm the diminishing returns from extending the separation channel.

I was initially interested in mapping the separation phase space of colloidal crystal / DNA separations. Early on, however, I noticed that in some cases, my crystals would have brightly refractive, colorful spots, contrasting with the usual dull shine of most of the crystals. We learned through laser diffraction that the bright regions were actually single grains, which naturally lead us to wonder if their presence affected performance. To answer this question, I minimized the time between scans to $\sim$4 sec by scanning over a smaller window, then ensured that the measurement window contained heterogeneous crystal. As explained in Chapter 3, my rapid scanning technique allowed me to generate enough snapshot data to emulate finish line data at any arbitrary point within the measurement window – a technique unparalleled for measuring local matrix effects on separation performance.

Chapter 4 toned down the data collection rates of Chapter 3 to answer a different but related question: what happens when we change the electric field during a separation? I wanted to know if we could find the different theorized mobility regimes for λ DNA in colloidal crystals. The results of Zeng and Harrison [9] left wanting to understand the behavior of very large DNA in these crystals. The best starting place would be to map the mobility vs. the applied electric field as there are many theories and predictions from gels and other microfluidic templates to compare against. Altering the electric field mid-separation would continue in the spirit of compressed data collection begun with Chapter 3, and also allowed for unique experimental controls by way of including the PCR marker separation. The result was unique data gathered by a technique that continues to prove its

versatility.

These techniques are not limited to colloidal crystal experiments. In any case where there exists a heterogeneous separation matrix, the method of Chapter 3 could be used to isolate local separation properties. In the case of bottom-up, self-assembled sieves, this technique to locate underperforming sections of material that could be further interrogated with other techniques to determine the root of the performance issues. If a device is designed with a gradient matrix to separate a wider variety of analytes, the effects of the gradient on each eluting band could be measured and quantified to monitor for any deleterious behaviors. Chapter 4 includes a method of visualizing and measuring the effect of changing separation parameters. While we tested only a varying electric field, one could alter buffer conditions, temperature, or other experimental values and observe the effects directly on the separation.

These techniques do not require an extraordinary amount of setup or experimental control to perform. They only require a method by which to tie the separation observations to the heterogeneous properties of concern. This low barrier to entry should leave the way open for future researchers to apply my techniques to their own unique investigations. I am sure that there are more innovations to be made using scanning mode measurements, and I look forward to seeing the field progress.

5.2 Future Work

Ideally, one would like to make single-molecule measurements of conformations and modes of motion [11], but this is not very straightforward in these devices. The first hurdle one might imagine is that the photonic behavior that led to the early work on colloidal crystals would prevent accurate measurement of the fluorescence of a dyed molecule. However, the photonic properties arise from an index of refraction mismatch between the colloid material and the inflitration fluid. Therefore, one can negate any photonic effects by matching the index of refraction of the running buffer with that of the colloids.

Of larger concern is the required depth of field to track a molecule through a crystal. To avoid any wall effects on crystal growth properties, the channel should be at least ten colloid diameters deep. However, the depth of field required to track a molecule in these devices runs counter to the ability to focus on small enough light sources. Recently developed lens-less CMOS technology may provide a unique solution to this issue and would be undoubtedly worth investigating [73, 74].

An alternative approach would be molecular simulation. The periodicity of colloidal

crystals lend themselves well to simulation space. Properly designed simulations similar to those used to unravel the dynamics of post-array separations would shed light on the specifics of the transport of DNA through these sieves. The insights gained would be invaluable in the eventual optimization of these crystals for more widespread application. If, as may be indicated in Figure 4.3, there are some molecules that remain infinitely separable, these devices may have an increased role to play in the future.

5.3 Conclusions

5.3.1 Summary

This thesis is an evaluation of the performance of colloidal crystals as DNA electrophoretic sieves. I evaluated a single type of colloids – 900 nm diameter silica – as it was the most common in separation literature and device fabrication. It is readily purchaseable off-the-shelf in highly-monodisperse batches for low cost. Without pretreatment of any kind, these colloids can be used to fabricate colloidal crystal packings in most microfluidic devices. Additionally, they have been shown [8,9,18,21] to be capable of DNA separations of lengths spanning over three orders of magnitude.

The central chapters of this thesis explored two aspects key to the future of colloidal crystals in DNA separation devices. Chapter 3 focused on the quality of crystal packing, while Chapter 4 explored the range of viable separations. In Chapter 3 I showed that, at least for sub-kilobasepair DNA, a separation-grade crystal can be made with grains of any size as long as the crystal remains close-packed. This result aligns well with the work of Mary Wirth's group on protein separations [10, 20, 23, 26], which relates nearly all performance gains to close-packing uniformity alone.

Chapter 4 builds on the work of Meistermann and Tinland [8], Zeng and Harrison [9], and Zhang and Wirth [22] to further map out the effect of the applied electric field on the mobility of both large and small DNA. We measured DNA separations of a PCR Marker ladder and λ-DNA while varying the applied electric field during elution. We found that between 4 and 80 V/cm, the mobility of sub-kilobasepair DNA is not affected by the electric field. Along with Chapter 3, this forms strong evidence that the separation of small DNA in colloidal crystals can be described by the Ogston sieving model [14–16].

Of particular interest was the field-dependence of the mobility of the λ-DNA, which was sigmoidal in characteristic. In fact, three regimes were clearly visible – a low-field, field independent regime; an intermediate linear field dependence; and a high field saturation

value of the mobility. The low-field regime which we confirmed was predicted by Meistermann and Tinland [8] but not observed. The transition between the first two regimes takes place at $E \approx 10$ V/cm, the lowest field measured by Meistermann and Tinland [8]. The linear regime matches that measured by Meistermann and Tinland [8] as well as the scaling predicted for the biased reptation with fluctuations model [66]. The observed delayed onset of the linear regime contributes towards an understanding of the separations of Zeng and Harrison [9] of a 13 kbp mixture from the 48.5 kbp λ-DNA. This linear region was also found by Zhang and Wirth [22] in 300 nm diameter silica colloids, as well as an approaching saturation value at high fields. We found our saturation crossover to be near 40 V/cm, which is similar to the scaled crossover they observed at 200 V/cm. This plateau region also aligns with predictions of the theoretical breakdown of the BRF model at high fields [66].

5.3.2 Impacts

The future of colloidal crystals in separation devices is uncertain. Mary Wirth has created a company, bioVidria, to commercialize silica colloidal crystals for ultra-high performance liquid chromatography. These columns take advantage of the low band broadening attributed to the close-packed crystals. There is not currently a product that takes advantage of the DNA separation capabilities of colloidal crystals. The work of the Harrison group with colloidal crystals moved from single-lane microfluidics to DNA prism continuous separation devices [18, 19, 21, 75]. Regardless of form factor, colloidal crystals continue to be used and studied for DNA separations. The DNA prism takes advantage of the self-assembly process to cover a large, 4×4 mm^2 area with sub-micron features – an ability not seen in any other mass-produceable devices.

The results I have presented in this thesis form important insights into the function and capability of colloidal crystals as DNA electrophoretic sieves. We now know that small DNA are unaffected by grain size, which lowers the quality control barrier for mass-fabrication of large-scale arrays. We know that large DNA behave in familiar ways but in higher ranges of electric fields. At the least, this knowledge enables faster separations than in comparable gels. Coupling the remarkable separation performance and ranges of colloidal crystals with their mechanical stability and ease of fabrication prepares them for a bright future in biomolecular separation.

References

[1] J. D. Watson and F. H. C. Crick. Molecular structure of nucleic acids. *Nature*, 171:737–738, 1953.

[2] S. Zamenhof, G. Brawerman, and E. Chargaff. On the desoxypentose nucleic acids from several microorganisms. *Biochim. Biophys. Acta*, 9:402–405, 1952.

[3] C. Heller, T. Duke, and J.-L. Viovy. Electrophoretic mobility of DNA in gels. II. Systematic experimental study in agarose gels. *Biopolymers*, 34:249–259, 1994.

[4] J.-L. Viovy. Electrophoresis of DNA and other polyelectrolytes: Physical mechanisms. *Rev. Mod. Phys.*, 72:813–872, 2000.

[5] Y. A. Vlasov, X. Z. Bo, J. C. Sturm, and D. J. Norris. On-chip natural assembly of silicon photonic bandgap crystals. *Nature*, 414:289–293, 2001.

[6] E. Kim, Y. Xia, and G. M. Whitesides. Two-and three-dimensional crystallization of polymeric microspheres by micromolding in capillaries. *Adv. Mater.*, 8:245–247, 1996.

[7] M. W. Barsoum. *Fundamentals of Ceramics*. Institute of Physics, London, 1997.

[8] L. Meistermann and B. Tinland. DNA electrophoresis in a monodisperse porous medium. *Phys. Rev. E*, 62:4014–4017, 2000.

[9] Y. Zeng and D. J. Harrison. Self-assembled colloidal arrays as three-dimensional nanofluidic sieves for separation of biomolecules on microchips. *Anal. Chem.*, 79:2289–2295, 2007.

[10] D. S. Malkin, B. Wei, A. J. Fogiel, S. L. Staats, and Wirth M. J. Submicrometer plate heights for capillaries packed with silica colloidal crystals. *Anal. Chem.*, 82:2175–2177, 2010.

[11] K. D. Dorfman, S. B. King, D. W. Olson, J. D. P. Thomas, and D R Tree. Beyond gel electrophoresis: Microfluidic separations, fluorescence burst analysis, and DNA stretching. *Chem. Rev.*, 113:2584–2667, 2013.

[12] D. Nathans and H. O. Smith. Restriction endonucleases in the analysis and restructuring of DNA molecules. *Annu. Rev. Biochem.*, 44:273–293, 1975.

[13] G. S. Hayward and M. G. Smith. The chromosome of bacteriophage T5: I. analysis of the single-stranded DNA fragments by agarose gel electrophoresis. *J. Mol. Biol.*, 63:383–395, 1972.

[14] A. G. Ogston. The spaces in a uniform random suspension of fibres. *Trans. Faraday Soc.*, 54:1754–1757, 1958.

[15] C. J. O. R. Morris. Gel filtration and gel electrophoresis. *Prot. Biol. Fluids*, 14:543–551, 1967.

[16] D. Rodbard and A. Chrambach. Estimation of molecular radius, free mobility, and valence using polyacrylamide gel electrophoresis. *Proc. Natl. Acad. Sci. U.S.A.*, 65:970–977, 1970.

[17] P. Pieranski. Colloidal crystals. *Contemporary Physics*, 24:25–73, 1983.

[18] N. Nazemifard, S. Bhattacharjee, J. H. Masliyah, and D. J. Harrison. DNA dynamics in nanoscale confinement under asymmetric pulsed field electrophoresis. *Angew. Chem. Int. Edit.*, 122:3398–3401, 2010.

[19] N. Nazemifard, L. Wang, W. Ye, S. Bhattacharjee, J. H. Masliyah, and D. J. Harrison. A systematic evaluation of the role of crystalline order in nanoporous materials on DNA separation. *Lab Chip*, 12:146–152, 2012.

[20] B. Wei, D. S. Malkin, and Wirth M. J. Plate heights below 50 nm for protein electrochromatography using silica colloidal crystals. *Anal. Chem.*, 82:10261–10221, 2010.

[21] Y. Zeng, M. He, and D. J. Harrison. Microfluidic self-patterning of large-scale crystalline nanoarrays for high-throughput continuous DNA fractionation. *Angew. Chem. Int. Edit.*, 47:6388–6391, 2008.

[22] H. Zhang and M. J. Wirth. Electromigration of single molecules of DNA in a crystalline array of 300-nm silica colloids. *Anal. Chem.*, 77:1237–1242, 2005.

[23] S. Zheng, E. Ross, M. A. Legg, and M. J. Wirth. High-speed electroseparations inside silica colloidal crystals. *J. Am. Chem. Soc.*, 128:9016–9017, 2006.

[24] J. D. Joannopoulos, P. R. Villeneuve, and S. Fan. Photonic crystals: putting a new twist on light. *Nature*, 386:143–149, 1997.

[25] D. J. Norris, E. G. Arlinghaus, L. Meng, R. Heiny, and L. E. Scriven. Opaline photonic crystals: How does self-assembly work? *Adv. Mater.*, 16:1393–1399, 2004.

[26] R. E. Birdsall, B. M. Koshel, Y. Hua, S. N. Ratnayaka, and M. J. Wirth. Modeling protein electrophoresis in silica colloidal crystals having brush layers of polyacrylamide. *Electrophoresis*, 34:753–760, 2013.

[27] H. Wei, L. Meng, Y. Jun, and D. J. Norris. Quantifying stacking faults and vacancies in thin convectively assembled colloidal crystals. *App. Phys. Lett.*, 89:241913, 2006.

[28] C. S. Effenhauser, A. Manz, and H. M. Widmer. Glass chips for high-speed capillary electrophoresis separations with submicrometer plate heights. *Anal. Chem.*, 65:2637–2642, 1993.

[29] R. C. Lo and V. M. Ugaz. Microchip DNA electrophoresis with automated whole-gel scanning detection. *Lab Chip*, 8:2135–2145, 2008.

[30] J. Wang, A. D. Gonzalez, and V. M. Ugaz. Tailoring bulk transport in hydrogels through control of polydispersivity in the nanoscale pore size distribution. *Adv. Mater.*, 20:4482–4489, 2008.

[31] K. D. Dorfman. DNA electophoresis in microfabricated devices. *Rev. Mod. Phys.*, 8:2903–2947, 2010.

[32] P. Jiang, J. F. Bertone, K. S. Hwang, and V. L. Colvin. Single-crystal colloidal multilayers of controlled thickness. *Chem. Mater.*, 11:2132–2140, 1999.

[33] G. A. Ozin and S. M. Yang. The race for the photonic chip: colloidal crystal assembly in silicon wafers. *Adv. Funct. Mater.*, 11:95–104, 2001.

[34] D. J. Norris and Y. A. Vlasov. Chemical approaches to three-dimensional semiconductor photonic crystals. *Adv. Mater.*, 13:371–376, 2001.

[35] C Lopez. Materials aspects of photonic crystals. *Adv. Mater.*, 15:1679–1704, 2003.

[36] L. R. Huang, J. O. Tegenfeldt, J. J. Kraeft, J. C. Sturm, R. H. Austin, and E. C. Cox. A DNA prism for high-speed continuous fractionation of large DNA molecules. *Nat. Biotechnol.*, 20:1048–1051, 2002.

[37] P. Schall. Laser diffraction microscopy. *Rep. Prog. Phys.*, 72:076601, 2009.

[38] R. L. Rill, B. R. Locke, Y. Liu, and D. H. van Winkle. Electrophoresis in lyotropic polymer liquid crystals. *Proc. Natl. Acad. Sci. U.S.A.*, 95:1534–1539, 1998.

[39] R. Svingen and B. Akerman. Mechanism of electrophoretic migration of DNA in the cubic phase of pluronic F127 and water. *J. Phys. Chem. B*, 108:2735–2743, 2004.

[40] S. C. Jacobson, R. Hergenroder, L. B. Koutny, R. J. Warmack, and J. M. Ramsey. Effects of injection schemes and column geometry on the performance of microchip electrophoresis devices. *Anal. Chem.*, 66:1107–1113, 1994.

[41] N. C. Stellwagen. Electrophoresis of DNA in agarose gels, polyacrylamide gels and in free solution. *Electrophoresis*, 30:188–195, 2009.

[42] G. W. Slater and H. L. Guo. An exactly solvable Ogston model of gel electrophoresis: I. The role of the symmetry and randomness of the gel structure. *Electrophoresis*, 17:977–988, 1996.

[43] G. W. Slater and H. L. Guo. An exactly solvable Ogston model of gel electrophoresis: II. Sieving through periodic gels. *Electrophoresis*, 17:1407–1415, 1996.

[44] G. W. Slater and J. R. Treurniet. An exactly solvable Ogston model of gel electrophoresis: III. Percolation and sieving through two-dimensional gels. *J. Chromatogr. A*, 772:39–48, 1997.

[45] J.-F. Mercier and G. W. Slater. An exactly solvable Ogston model of gel electrophoresis: IV. Sieving through periodic three-dimensional gels. *Electrophoresis*, 19:1560–1565, 1998.

[46] J. Labrie, J.-F. Mercier, and G. W. Slater. An exactly solvable Ogston model of gel electrophoresis: V. Attractive gel-analyte interactions and their effects on the Ferguson plot. *Electrophoresis*, 21:823–833, 2000.

[47] J. Boileau and G. W. Slater. An exactly solvable Ogston model of gel electrophoresis: VI. Towards a theory for macromolecules. *Electrophoresis*, 22:673–683, 2001.

[48] J.-F. Mercier and G. W. Slater. An exactly solvable Ogston model of gel electrophoresis: VII. Diffusion and mobility of hard spherical particles in three-dimensional gels. *Macromolecules*, 34:3437–3445, 2001.

[49] J.-F. Mercier, F. Tessier, and G. W. Slater. An exactly solvable Ogston model of gel electrophoresis: VIII. Nonconducting gel fibers, curved field lines, and the Nernst-Einstein relation. *Electrophoresis*, 22:2631–2638, 2001.

[50] M. G. Gauthier and G. W. Slater. An exactly solvable Ogston model of gel electrophoresis: IX. Generalizing the lattice model to treat high field intensities. *J. Chem. Phys.*, 117:6745–6756, 2002.

[51] M. G. Gauthier and G. W. Slater. An exactly solvable Ogston model of gel electrophoresis: X. Application to high-field separation techniques. *Electrophoresis*, 24:441–451, 2003.

[52] M. G. Gauthier, G. W. Slater, and K. D. Dorfman. Exact lattice calculations of dispersion coefficients in the presence of external fields and obstacles. *Eur. Phys. J. E*, 15:71–82, 2004.

[53] M. Rubinstein and R. H. Colby. *Polymer Physics*. Oxford University Press, New York, 2003.

[54] C. Bustamante, J. F. Marko, E. D. Siggia, and S. Smith. Entropic elasticity of λ phage DNA. *Science*, 265:1599–1600, 1994.

[55] T. T. Perkins, D. E. Smith, R. G. Larson, and S. Chu. Stretching of a single tethered polymer in a uniform flow. *Science*, 268:83–87, 1995.

[56] O. B. Bakajin, T. A. J. Duke, C. F. Chou, S. S. Chan, R. H. Austin, and E. C. Cox. Electrohydrodynamic stretching of DNA in confined environments. *Phys. Rev. Lett.*, 80:2737–2740, 1998.

[57] G. C. Randall and P. S. Doyle. DNA deformation in electric fields: DNA driven past a cylindrical obstruction. *Macromolecules*, 38:2410–2418, 2005.

[58] N. Laachi, C. Declet, C. M. Matson, and K. D. Dorfman. Nonequilibrium transport of rigid macromolecules in periodically constricted geometries. *Phys. Rev. Lett.*, 98:098106, 2007.

[59] H. Yamakawa and M. Fujii. Translational friction coefficient of wormlike chains. *Macromolecules*, 6:407–415, 1973.

[60] N. C. Stellwagen, C. Gelfi, and P. G. Righetti. The free solution mobility of DNA. *Biopolymers*, 42:687–703, 1997.

[61] A. van Blaaderen, R. Ruel, and P. Wiltzius. Template-directed colloidal crystallization. *Nature*, 385:321–324, 1997.

[62] Y. Yin, Y. Lu, B. Gates, and Y. Xia. Template-assisted self-assembly: a practical route to complex aggregates of monodispersed colloids with well-defined sizes, shapes, and structures. *J. Am. Chem. Soc.*, 123:8718–8729, 2001.

[63] S. B. King and K. D. Dorfman. Role of order during ogston sieving of DNA in colloidal crystals. *Anal. Chem.*, 85:7769–7776, 2013.

[64] O. J. Lumpkin, P. Déjardin, and B. H. Zimm. Theory of gel electrophoresis of DNA. *Biopolymers*, 24:1573–1593, 1985.

[65] G. W. Slater and J. Noolandi. New biased-reptation model for charged polymers. *Phys. Rev. Lett.*, 55:1579, 1985.

[66] T. A. J. Duke, A. Semenov, and J.-L. Viovy. Mobility of a reptating polymer. *Phys. Rev. Lett.*, 69:3260–3263, 1992.

[67] T. Duke, J.-L. Viovy, and A. N. Semenov. Electrophoretic mobility of DNA in gels. I. New biased reptation theory including fluctuations. *Biopolymers*, 34:239–247, 1994.

[68] P.-G. De Gennes. *Scaling concepts in polymer physics*. Cornell University Press, 1979.

[69] G. C. Randall and P. S. Doyle. Permeation-driven flow in poly (dimethylsiloxane) microfluidic devices. *Proc. Natl. Acad. Sci. U.S.A.*, 102:10813–10818, 2005.

[70] J. Ou, J. Cho, D. W. Olson, and K. D. Dorfman. DNA electrophoresis in a sparse ordered post array. *Phys. Rev. E*, 79:061904, 2009.

[71] N. Laachi and K. D. Dorfman. DNA electrophoresis in confined, periodic geometries: A new lakes-straits model. *J. Chem. Phys.*, 133:234104, 2010.

[72] S.-G. Park, D. W. Olson, and K. D. Dorfman. DNA electrophoresis in a nanofence array. *Lab Chip*, 12:1463–1470, 2012.

[73] A. Ozcan and U. Demirci. Ultra wide-field lens-free monitoring of cells on-chip. *Lab Chip*, 8:98–106, 2008.

[74] A. Greenbaum, W. Luo, T.-W. Su, Z. Göröcs, L. Xue, S. O. Isikman, A. F. Coskun, O. Mudanyali, and A. Ozcan. Imaging without lenses: achievements and remaining challenges of wide-field on-chip microscopy. *Nat. Methods*, 9:889–895, 2012.

[75] N. Nazemifard, S. Bhattacharjee, J. H. Masliyah, and D. J. Harrison. Nonmonotonous variation of DNA angular separation during asymmetric pulsed field electrophoresis. *Electrophoresis*, 34:2453–2463, 2013.

Appendix A

Protocols

A.1 Polymerase Chain Reaction

1. If you have not already done so, prepare a desalted DNA solution. The PCR reaction will not work in the presence of extra salts.

   (a) If you are using a primer, first digest the template with a single-cut enzyme (check on New England Biolabs for the different enzyme/plasmid combinations) to prevent snap-back rehybridization during PCR. It is possible to do PCR with the circular DNA too, but it is more efficient with the linear DNA.

   (b) Use a min-elute column to remove the salts and the restriction enzyme. These elute in a 10 uL volume of water . If you overload the column (by digesting too much DNA), then you should get approximately 5 ug of DNA out of the column, to give you 0.5 ug/ml.

   (c) Dilute the DNA down to 0.5 to 5 ng/uL for the PCR. Be sure to dilute in water.

2. If you have not already done so, prepare a stock solution of the left and right primers at 10 uM concentration.

   (a) Dissolve the oligos received from the synthesis in 100 uL of water. Normally you should have approximately 10 nmoles of oligo, which would make a 100 uM solution.

   (b) Vortex and centrifuge to dissolve the oligos.

   (c) Make the 10 uM stock solution by taking 1 uL of your dissolved oligo and adding the appropriate amount of water. The uL of water needed is given by (conc in

uM/10)-1. For example, with a 100 uM solution you would take 1 uL of dissolved oligos and add 9 uL of water.

3. Check if you have an aliquot of the TAQ mix available in the fridge.
   - TAQ 2x mix is stable for 3 months at 4 C. The stock should only be defrosted no more that 15 times to have reliable results.
   - If there is stable TAQ 2x in the fridge, use it. If not, make a new aliquot for the fridge by thawing the mix.
4. Prepare the PCR mixture. Prior to adding any DNA solutions, be sure to vortex and pipet mix before pipetting. For the TAQ mix, which has surfactants, simply invert the tube a few times to mix. Do not vortex the TAQ or you will get lots of foam.
   - Add 5 uL of each primer at 10 uM (total of 10 uL).
   - Add 1 uL of your DNA at 0.5-5 ng/uL.
   - Add 14 uL of DI water to bring the volume to 25 uL.
   - Add 25 uL of TAQ mix.
5. Run the PCR reaction. The standard cycling is:
   (a) 94°C for 5 minutes.
   (b) 40 cycles of:
      i. 94°C for 30 sec.
      ii. primer annealing temp. for 30 sec. For DNAzyme substrate primers, T = 50°C.
      iii. 72°C for 1 minute per kbp. For pUC19 DNAzyme amplicon (1275 bp), use 1 minute.
      iv. 68°C for 5 minutes.
      v. 15°C indefinitely until you stop the reaction.
6. Check the product on a gel. If you are doing a 1 kbp sized amplicon, use 1% agarose at 100 V for approximately 90 minutes.

A.2 Ethanol precipitation of DNA

Adapted from:
The Condensed Protocols

From *Molecular Cloning: A Laboratory Manual*
Sambrook and Russell
CSHL Press, 2006.

1. Estimate the volume of the DNA solution.

2. Adjust the concentration of monovalent cations either by dilution with TE (pH 8.0) if the DNA solution contains a high concentration of salts or by addition of one of the salt solutions shown in Table A.1.

3. Mix the solution well. Add exactly 2 volumes of ice-cold ethanol and again mix the solution well. Store the ethanolic solution on ice to allow the precipitate of DNA to form.

   - Usually 15-30 minutes is sufficient, but when the size of the DNA is small ($<$ 100 nucleotides) or when it is present in small amounts ($<$ 0.1 μg/ml), extend the period of storage to at least 1 hour and add $MgCl_2$ to a final concentration of 0.01 M.
   - DNA can be stored indefinitely in ethanolic solutions in sealed tubes at 0°C or -20°C.

4. Recover the DNA by centrifugation at 0°C.

5. Carefully remove the supernatant with an automatic micropipettor or a disposable pipette tip attached to a vacuum line. Take care not to disturb the pellet of nucleic acid (which may be invisible). Use the pipette tip to remove any drops of fluid that adhere to the walls of the tube.

6. Fill the tube half way with 70% ethanol and recentrifuge at maximum speed for 2 minutes at 4°C in a microfuge.

7. Repeat Step 5.

Salt	Stock Solution (M)	Final Concentration (M)
Ammonium acetate	10.0	2.0-2.5
Lithium chloride	8.0	0.8
Sodium chloride	5.0	0.2
Sodium acetate	3.0 (pH 5.2)	0.3

Table A.1: Common salts used in preparation of DNA solutions for precipitation with ethanol.

8. Store the open tube on the bench at room temperature until the last traces of fluid have evaporated.

9. Dissolve the DNA pellet (which is often invisible) in the desired volume of buffer (usually TE [pH between 7.6 and 8.0]) Rinse the walls of the tube well with the buffer.

Appendix B

Reptation Data

Table B.1: The collected mobility data used in generating Figure 4.3. The "binned" value of the electric field is the value that was sent to the voltage controller. The "actual" electric field is calculated from the measured potentials in each reservoir. The mobility data is calculated using the method described in Figure 4.2.

4	2.7	-0.083±0.449	-0.552±0.067	-0.219±0.170	-0.157±0.237	0.307±0.121
	2.8	0.603±0.060	1.914±0.019	1.587±0.023	2.070±0.017	
	3.0	-0.298±0.111	-0.650±0.051	-0.090±0.366	0.357±0.093	0.504±0.066
	3.2	-0.523±0.059	0.611±0.051	1.002±0.031	1.629±0.019	0.592±0.052
	4.2	1.397±0.017	1.446±0.016	1.274±0.019		
	4.2	0.130±1.404	1.306±0.023	1.366±0.021	1.543±0.018	1.292±0.023
	4.2	0.210±0.113	0.816±0.029	0.923±0.026	1.022±0.023	1.356±0.017
	4.3	-0.053±8.458	0.243±0.408	0.228±0.459	0.233±0.441	0.174±0.786
5	6.4	0.070±0.223	0.250±0.063	0.379±0.041	0.564±0.028	0.803±0.020
	7.2	-0.437±0.032	0.762±0.018	0.872±0.016	0.832±0.017	0.766±0.018

Electric Field, V/cm		Mobility, cm·μm/V·s				
Binned	Actual	λ-DNA	750 bp	500 bp	300 bp	150 bp
7	5.6	-0.098±0.182	0.549±0.032	0.804±0.022	1.085±0.016	0.426±0.042
	5.7	-0.142±0.123	0.542±0.032	0.597±0.029	0.955±0.018	1.595±0.011
	5.7	0.251±0.070	0.387±0.045	0.449±0.039	0.488±0.036	0.567±0.031
	5.9	0.125±0.137	0.937±0.018	1.131±0.015	1.157±0.015	1.030±0.017
	5.9	0.095±0.179	0.180±0.094	0.178±0.095	0.159±0.107	0.195±0.087
	6.1	0.217±0.076	0.399±0.041	0.485±0.034	0.309±0.053	0.201±0.082
	7.0	0.256±0.056	0.680±0.021	0.874±0.016	0.886±0.016	0.933±0.015
	7.0	0.237±0.262	0.569±0.051	0.677±0.038	0.747±0.032	1.046±0.019
	7.0	0.074±2.613	0.393±0.099	0.560±0.052	0.692±0.036	0.745±0.032
	7.2	0.275±0.050	0.614±0.022	0.701±0.020	0.849±0.016	0.842±0.016
	8.2	-0.087±0.139	0.657±0.018	0.835±0.015	1.066±0.011	1.260±0.010
	9.1	0.700±0.016	0.651±0.017	0.635±0.017	0.639±0.017	0.791±0.014
10	8.6	0.413±0.028	0.589±0.020	0.612±0.019	0.635±0.018	0.684±0.017
	8.7	0.340±0.034	0.468±0.025	0.502±0.023	0.524±0.022	0.543±0.021
	9.0	0.384±0.029	0.646±0.017	0.709±0.016	0.764±0.015	0.797±0.014
	9.9	0.317±0.105	0.674±0.027	0.766±0.022	0.853±0.018	0.912±0.016
	10.0	0.334±0.030	0.667±0.015	0.774±0.013	0.876±0.011	0.914±0.011
	11.1	0.520±0.017	0.749±0.012	0.823±0.011	0.904±0.010	0.892±0.010
12	13.1	0.161±0.048	0.456±0.017	0.629±0.012	0.771±0.010	0.896±0.009
	13.8	0.362±0.020	0.740±0.010	0.629±0.011	0.655±0.011	0.781±0.009
15	16.6	0.336±0.018	0.480±0.013	0.533±0.011	0.606±0.010	0.641±0.009

Electric Field, V/cm		Mobility, cm·μm/V·s				
Binned	Actual	λ-DNA	750 bp	500 bp	300 bp	150 bp
16	14.2	0.170±0.042	0.862±0.008	0.911±0.008	1.045±0.007	1.429±0.005
	14.4	0.341±0.020	0.449±0.015	0.516±0.013	0.563±0.012	0.661±0.011
	14.6	0.048±0.142	0.724±0.009	1.029±0.007	1.016±0.007	1.151±0.006
	14.7	0.394±0.017	0.802±0.009	0.830±0.008	1.059±0.006	0.880±0.008
	14.7	0.345±0.020	0.428±0.016	0.463±0.015	0.378±0.018	0.517±0.013
	14.7	0.234±0.029	0.295±0.023	0.311±0.022	0.330±0.021	0.343±0.020
	15.5	0.352±0.055	0.720±0.015	0.833±0.012	0.927±0.010	0.977±0.009
	15.6	0.413±0.041	0.636±0.019	0.673±0.017	0.753±0.014	0.694±0.016
	15.7	0.305±0.021	0.638±0.010	0.741±0.009	0.789±0.008	1.008±0.006
	15.7	0.457±0.014	0.673±0.009	0.768±0.008	0.822±0.008	0.891±0.007
18	18.6	0.278±0.019	0.440±0.012	0.563±0.010	0.711±0.008	0.809±0.007
	19.5	0.381±0.013	0.764±0.007	0.716±0.007	0.767±0.007	0.660±0.008
20	17.9	0.167±0.033	0.399±0.014	0.731±0.008	0.806±0.007	0.972±0.006
	18.0	0.421±0.013	0.430±0.013	0.481±0.012	0.552±0.010	0.612±0.009
	18.2	0.255±0.022	0.851±0.006	0.957±0.006	1.010±0.005	0.893±0.006
	18.3	0.400±0.014	0.471±0.012	0.506±0.011	0.322±0.017	0.470±0.012
	18.5	-0.002±3.661	0.656±0.008	0.745±0.007	0.950±0.006	0.825±0.007
	18.6	0.295±0.018	0.352±0.015	0.359±0.015	0.386±0.014	0.396±0.014
	19.3	0.418±0.012	0.588±0.009	0.770±0.007	0.879±0.006	0.898±0.006
	19.3	0.438±0.029	0.664±0.014	0.719±0.012	0.779±0.011	0.796±0.010
	19.4	0.230±0.100	0.509±0.022	0.629±0.015	0.735±0.012	0.760±0.011
	19.5	0.528±0.010	0.705±0.007	0.796±0.006	0.862±0.006	0.949±0.005

Electric Field, V/cm		Mobility, cm·μm/V·s				
Binned	Actual	λ-DNA	750 bp	500 bp	300 bp	150 bp
25	25.3	0.538±0.007	0.569±0.007	0.599±0.007	0.623±0.006	0.628±0.006
	26.2	0.379±0.010	0.506±0.008	0.557±0.007	0.624±0.006	0.549±0.007
27	24.5	0.263±0.016	0.255±0.016	0.645±0.006	0.799±0.005	0.847±0.005
	24.7	0.510±0.008	0.497±0.008	0.510±0.008	0.563±0.007	0.639±0.006
	25.0	0.487±0.008	0.559±0.007	0.573±0.007	0.598±0.007	0.269±0.015
	25.0	0.294±0.014	0.743±0.005	0.886±0.005	0.964±0.004	1.083±0.004
	25.4	0.106±0.037	0.550±0.007	0.688±0.006	0.878±0.004	0.895±0.004
	25.5	0.398±0.010	0.433±0.009	0.444±0.009	0.457±0.009	0.481±0.008
	26.0	0.380±0.029	0.529±0.016	0.547±0.015	0.648±0.011	0.707±0.009
	26.0	0.464±0.008	0.707±0.005	0.765±0.005	0.814±0.005	0.964±0.004
	26.1	0.534±0.015	0.729±0.009	0.771±0.008	0.829±0.007	0.837±0.007
	26.1	0.565±0.007	0.752±0.005	0.808±0.005	0.887±0.004	0.918±0.004
30	30.0	0.606±0.006	0.678±0.005	0.676±0.005	0.693±0.005	0.701±0.005
	30.5	0.586±0.006	0.362±0.009	0.355±0.009	1.186±0.003	
	30.9	0.416±0.008	0.544±0.006	0.590±0.005	0.651±0.005	0.801±0.004
35	32.1	0.292±0.011	0.379±0.008	0.333±0.009	0.671±0.005	0.601±0.005
	32.4	0.317±0.010	0.757±0.004	0.882±0.004	0.934±0.003	1.003±0.003
	33.1	0.203±0.015	0.481±0.006	0.618±0.005	0.732±0.004	0.886±0.003
	33.6	0.587±0.005	0.771±0.004	0.759±0.004	0.832±0.004	0.926±0.003
	33.6	0.462±0.015	0.568±0.011	0.581±0.010	0.669±0.008	0.737±0.007
	33.6	0.540±0.012	0.811±0.006	1.011±0.004	0.899±0.005	

Electric Field, V/cm		Mobility, cm·μm/V·s				
Binned	Actual	λ-DNA	750 bp	500 bp	300 bp	150 bp
43	42.1	0.403±0.006	0.625±0.004	0.700±0.003	0.780±0.003	0.835±0.003
	43.1	0.667±0.003	0.621±0.004	0.587±0.004	0.636±0.004	0.676±0.003
47	43.2	0.521±0.004	0.959±0.002	1.006±0.002	1.101±0.002	0.907±0.003
	43.5	0.384±0.006	0.462±0.005	0.443±0.005	0.326±0.007	0.576±0.004
	43.7	0.409±0.006	0.639±0.004	0.766±0.003	0.814±0.003	1.016±0.002
	44.7	0.490±0.010	0.804±0.004	0.833±0.004	0.914±0.004	0.935±0.004
	44.8	0.561±0.008	0.676±0.006	0.681±0.006	0.696±0.006	0.731±0.005
	44.8	0.861±0.003	0.855±0.003	0.879±0.003	0.623±0.004	
	44.9	0.251±0.009	0.288±0.008	0.368±0.006	0.536±0.004	0.675±0.003
	45.0	0.654±0.003	0.458±0.005	0.749±0.003	0.835±0.003	0.846±0.003
60	55.8	0.362±0.005	0.837±0.002	0.929±0.002	0.998±0.002	1.053±0.002
	55.8	0.427±0.004	0.527±0.003	0.540±0.003	0.567±0.003	0.507±0.004
	56.2	0.540±0.003	0.474±0.004	0.480±0.004	0.741±0.002	0.846±0.002
	57.1	0.543±0.003	0.845±0.002	0.887±0.002	0.930±0.002	0.996±0.002
	57.1	0.564±0.006	0.776±0.004	0.813±0.003	0.843±0.003	0.914±0.003
	57.2	0.721±0.002	0.864±0.002	0.794±0.002	0.637±0.003	0.807±0.002
	57.2	0.629±0.005	0.773±0.004	0.773±0.004	0.776±0.004	0.781±0.004
	57.6	0.322±0.005	0.896±0.002	0.968±0.002	0.943±0.002	1.104±0.002
	57.6	0.384±0.005	0.368±0.005	0.373±0.005	0.392±0.004	0.419±0.004
	58.0	0.407±0.004	0.772±0.002	0.831±0.002	0.913±0.002	0.931±0.002
	59.0	0.871±0.002	0.655±0.003	0.637±0.003	0.843±0.002	1.060±0.002

Electric Field, V/cm		Mobility, cm·μm/V·s				
Binned	Actual	λ-DNA	750 bp	500 bp	300 bp	150 bp
80	76.9	0.569±0.002	0.643±0.002	0.652±0.002	0.661±0.002	0.683±0.002
	77.9	0.523±0.002	0.793±0.002	0.846±0.002	0.871±0.001	0.879±0.001